Photometric Method for Radiometric Correction of Multispectral Scanner Data*

by

R.J. WOODHAM** & T.K. LEE

Technical Report 84-14
October 1984

Laboratory for Computational Vision
Department of Computer Science
University of British Columbia
Vancouver, B.C., CANADA

Abstract

Radiometric correction of multispectral scanner data requires physical models of image formation in order to deal with variations in topography, scene irradiance, atmosphere and viewing conditions. The scene radiance equation is more complex for rugged terrain than for flat terrain since it must model elevation, slope and aspect dependent effects. A simple six parameter model is presented to account for differential amounts of solar irradiance, sky irradiance and path radiance across a scene. The model uses the idea of a reflectance map to represent scene radiance as a function of surface orientation. Scene radiance is derived from the bidirectional reflectance distribution function (BRDF) of the surface material and a distribution of light sources. The sun is treated as a collimated source and the sky is treated as a uniform hemispherical source. The atmosphere adds further complication and is treated as an optically thin, horizontally uniform layer.

The required six parameters account for atmospheric effects and can be estimated when a suitable digital terrain model (DTM) is available. This is demonstrated for Landsat MSS images using a test site near St. Mary Lake in southeastern British Columbia. An intrinsic surface albedo is estimated at each point, independent of how that point is illuminated and viewed.

It is argued that earlier conclusions about the usefulness of the Lambertian assumption for the radiometric correction of multispectral scanner data were premature. Correction methods proposed in the literature fail even if the surface is Lambertian. This is because sky irradiance is significant and must be dealt with explicitly, especially for slopes approaching the grazing angle of solar incidence.

* submitted to *Canadian Journal of Remote Sensing*
** R.J. Woodham is a Fellow of the Canadian Institute for Advanced Research.

INTRODUCTION

Remote sensing benefits when multiple satellite data sets are made directly comparable. One problem is to determine a geometric transformation to map positions in one data to those in another. But, radiometric correction is also required when the spectral measurements in one data set are to be directly compared to those in another. Early attempts at Landsat radiometric correction provided calibrated radiance values, primarily motivated by the need to directly compare data obtained from different sites and at different times (Ahern & Murphy (1978)), (Robinove (1982)). In areas of rugged terrain, radiometric correction is required even if the measurements in one data set are to be directly compared only to those from other locations in the same data set. Other attempts at Landsat radiometric correction account for the local dependence of scene radiance on topography and atmosphere (Justice *et al.* (1980)), (Smith *et al.* (1980)), (Shibata *et al.* (1981)), (Sjoberg (1982)), (Teillet *et al.* (1982)).

Before a direct comparison of multiple satellite data sets is attempted, it is important to identify what it is that is being compared. Ideally, the comparison would show changes in an intrinsic scene property and be invariant to other effects. But, sensor measurements result from the interaction of several factors. Suppose the intrinsic property of interest is ground cover. The effects of surface material and topography must be separated from each other and from the effects of illumination, shadows, viewing direction and path phenomena. This paper describes a method for radiometric correction that uses a physical model of image formation to disambiguate the effects of ground cover, topography, direct solar irradiance, diffuse sky irradiance and path radiance. The result is an "albedo map" that determines an intrinsic scene property related to ground cover. Geocoded albedo maps would be directly comparable since variations due to topography, illumination and path phenomena are removed.

The method first corrects for path radiance by estimating path radiance as an exponential function of elevation. The atmosphere is treated as an optically thin, horizontally homogeneous layer allowing optical thickness also to be estimated as an exponential function of elevation. The sun is treated as a collimated source of constant irradiance at the top of the atmosphere and the sky is treated as a uniform hemispherical source with radiance estimated as an exponential function of elevation. Atmospheric parameters that determine the relative components of direct sun and diffuse sky irradiance at the target are estimated using one of three methods. First, since the required parameters correspond to physical quantities, values can be obtained from the literature or derived from proposed standard atmospheres (Valley (1965)). Second, direct measurements are made across cast shadow boundaries where the underlying ground cover remains constant. Third, direct measurements are made from shadowed areas of known albedo. It is shown that diffuse sky illumination is significant and cannot be ignored for radiometric correction in the shorter wavelength bands. Once the parameters are estimated, the albedo map is produced for direct comparison to ground cover.

The approach uses the idea of a reflectance map to represent scene radiance as a function of surface orientation. Reflectance maps provide a uniform representation for comparing different models of surface reflectance and different conditions of illumination. The reflectance map is here derived from the bidirectional reflectance distribution function (BRDF) and a given light source distribution. The BRDF characterizes the intrinsic reflectance properties of a surface material.

The approach is demonstrated using Landsat MSS imagery of a test site near St. Mary Lake in southeastern British Columbia. For this test site, topographic effects dominate. Figure 1 compares a portion of a Landsat MSS band 7 image with a hill-shaded rendering of the underlying terrain computed from a corresponding DTM. The correlation coefficient between

the two images is 0.737 indicating that a simple linear model gives a good prediction of measured brightness as a function of the cosine of the angle of incidence of the direct solar beam.

Estimating ground cover by direct comparison of multitemporal data will suffer unless the images are acquired under similar conditions of illumination. Figure 2 compares the hill-shaded rendering of Figure 1(b) to that corresponding to a time of satellite overpass five hours later. The correlation coefficient between images is now -0.049 indicating that no linear model will account for the difference in measured brightness even if the ground cover remains constant. Indeed, it can be shown that two images acquired under identical viewing geometries but varying conditions of illumination provide independent measurements related to slope and aspect. This idea has been exploited in a technique called photometric stereo (Woodham (1980a)) that is used to determine part position and orientation in automatic assembly (Horn & Ikeuchi (1984)).

In remote sensing, one attempts to interpret multispectral scanner data directly in terms of ground cover. Radiometric correction for topographic and atmospheric effects makes this direct interpretation possible. Interestingly, industrial applications of image analysis interpret variations in scene radiance directly in terms of object shape. This is possible when objects have uniform optical properties (Horn (1975)), (Horn (1977)), (Ikeuchi & Horn (1981)), (Woodham (1981)). Separating changes in scene radiance due to topography from changes due to ground cover is difficult because trade-offs emerge that cannot be resolved in a single view. Nevertheless, there have been some attempts to extract both topographic and ground cover information from multispectral images (Eliason *et al.* (1981)), (Haralick & Wang (1983)).

LIST OF SYMBOLS

Symbol	Name	Description	Units
$F(\alpha,\beta;\gamma;z)$	hypergeometric series	see Appendix B	
H_τ	scale height	scale height for optical thickness	m^{-1}
H_P	scale height	scale height for path radiance	m^{-1}
H_S	scale height	scale height for sky radiance	m^{-1}
T_d	transmission	downward transmission through atmosphere	
T_u	transmission	upward transmission through atmosphere	
$f_r(\theta_i,\phi_i;\theta_r,\phi_r)$	BRDF	bidirectional reflectance distribution function	sr^{-1}
$f_r(\theta_i,\phi_i;\theta_r,\phi_r;\lambda)$	spectral BRDF	spectral bidirectional reflectance distribution function	sr^{-1}
$f_r(\lambda)$	relative spectral BRDF	separable relative spectral bidirectional reflectance distribution function	
$\Gamma(x)$	gamma function	see Appendix B	
β	volume extinction coefficient	atmospheric extinction coefficient, including Rayleigh scattering, Mie scattering and ozone absorption	m^{-1}
$\delta(x)$	Dirac delta function	$\delta(x) = 0$ for $x \neq 0$; $\int \delta(x)dx = 1$; $\int f(x)\delta(x-a)dx = f(a)$	
ρ	albedo	fraction of radiant flux reflected compared to that of ideal Lambertian surface irradiated in exactly the same way	
τ	optical thickness	fraction of radiant flux transmitted along a given path	
τ_0		sea-level value of optical thickness	

i, e, g	photometric angles	representation for direction; i, e and g are respectively the incident, exitant and phase angles	
(θ,ϕ)	spherical coordinates	representation for direction; θ is the polar angle measured from the Z-axis and ϕ is the azimuth angle measured counter-clockwise from the X-axis	
(p, q)	gradient coordinates	representation for direction; $p = \partial f(x,y)/\partial x$ and $q = \partial f(x,y)/\partial y$	
$z = f(x, y)$	DTM	digital terrain model; surface elevation in an earth-centred coordinate system	m
Φ	radiant flux	power propagated as optical electromagnetic radiation	mW
E	irradiance	incident flux (surface) density	$mW \cdot cm^{-2}$
E_0		irradiance of a collimated source measured perpendicular to the direction of propagation	$mW \cdot cm^{-2}$
E_S		sky irradiance	$mW \cdot cm^{-2}$
E_{S0}		sky irradiance at sea level	$mW \cdot cm^{-2}$
M	radiant exitance	exitant flux (surface) density	$mW \cdot cm^{-2}$
L	radiance	radiant flux measured per unit surface area per unit projected solid angle	$mW \cdot cm^{-2} \cdot sr^{-1}$
L_0		radiance of a hemispherical uniform source	$mW \cdot cm^{-2} \cdot sr^{-1}$
L_P		path radiance	$mW \cdot cm^{-2} \cdot sr^{-1}$
L_{P0}		path radiance at sea level	$mW \cdot cm^{-2} \cdot sr^{-1}$
Ω		projected solid angle	sr
ω		solid angle	sr

THE REFLECTANCE MAP

The amount of light reflected by a surface element in a given direction depends on its optical properties, on its microstructure and on the spatial and spectral configuration of the light sources. For most surfaces, the fraction of the total irradiance reflected towards the sensor depends only on the surface orientation. The reflectance map $R(p,q)$, introduced by Horn (1977), determines scene radiance as a function of the surface gradient (p,q). A reflectance map is a useful representation because it compiles the relevant information about surface material, light source distribution and viewer position into a single function.

Reflectance maps can be measured directly using a goniometer mounted sample or indirectly from the image of a calibration object of known shape (Woodham (1978)). A reflectance map may also be calculated if the properties of the surface material and the distribution of light sources is given (Horn & Sjoberg (1979)). Intrinsic reflectance properties of a surface material are specified by the bidirectional reflectance distribution function (BRDF) of Nicodemus *et al.* (1977). In this section, we consider the BRDF of a Lambertian surface and of a class of surfaces identified by Minnaert (1941). Reflectance maps are presented both for a collimated light source and a uniform hemispherical source.

Coordinate Systems

It is convenient to distinguish three different coordinate systems. The BRDF is specified in an object-centred coordinate system defined with respect to a plane tangent to the surface at a point of interest. Image acquisition and the reflectance map are specified in a viewer-centred coordinate system. Digital terrain models, and other geocoded reference data, are specified in an earth-centered coordinate system. It is possible to define each of these coordinate systems independently and to develop full transformation equations from one to the other. To relate the

incident and reflected ray geometry, it is sufficient to develop transformation equations for directions only. There are several equivalent ways to define directions within a given coordinate system. The development here is based on spherical coordinates (θ,ϕ) shown in Figure 3. The polar or zenith angle θ is measured from the Z-axis and the azimuth angle ϕ is measured counter-clockwise from the X-axis in the XY plane. (In navigation, azimuth is usually measured clockwise from north and the elevation angle is used instead of the zenith angle. These are the complements of the angles given here.)

First, consider a plane tangent to the surface at a point of interest. A local reference direction is chosen in the tangent plane and a Cartesian coordinate system is erected with the X-axis aligned with the reference direction and with the Z-axis aligned with the surface normal. Four angles (θ_i,ϕ_i) and (θ_r,ϕ_r) are required to specify an arbitrary incident and reflected ray geometry as shown in Figure 4. Often, one considers materials whose reflectance characteristics are invariant with respect to rotations about the surface normal. This is equivalent to saying that only the difference in azimuth $(\phi_r - \phi_i)$ is required since the choice of a reference direction for the X-axis is arbitrary. For surfaces that are isotropic in this way, only three angles are required to specify the incident and reflected ray geometry. Figure 5 illustrates another way to specify these three angles. Clearly $i = \theta_i$ and $e = \theta_r$. Applying the cosine law for the sides of the spherical triangle shown in Figure 6, one obtains

$$\cos g = \cos\theta_i \cos\theta_r + \sin\theta_i \sin\theta_r \cos(\phi_r - \phi_i) \qquad (1)$$

Equation (1) is used to determine the phase angle g from the corresponding $(\phi_r - \phi_i)$ and vice-versa.

Next, let the image plane define the reference plane with the Z-axis aligned to the viewing direction. For a distant viewer and a distant light source, this viewer-centred coordinate system is a global coordinate system in the sense that the directions of the incident and the reflected

ray can be specified independently from the surface normal at local points of interest. Let (θ_n, ϕ_n) be the direction of a particular surface normal and let (θ, ϕ) be any other direction, both specified in the viewer-centred coordinate system. Using the spherical triangle of Figure 7 and following Horn & Sjoberg (1979), one obtains

$$\begin{aligned} \cos\theta' &= \cos\theta\cos\theta_n + \sin\theta\sin\theta_n\cos(\phi - \phi_n) \\ \sin\theta'\sin(\phi_r - \phi') &= \sin\theta\sin(\phi - \phi_n) \\ \sin\theta'\cos(\phi_r - \phi') &= \cos\theta\sin\theta_n - \sin\theta\cos\theta_n\cos(\phi - \phi_n) \end{aligned} \tag{2}$$

Equation (2) is used to transform the direction (θ, ϕ) into the object-centred coordinate system where it becomes (θ', ϕ'). In particular, Equation 2 allows us to determine the local incident direction (θ_i, ϕ_i) from a global source direction (θ_0, ϕ_0).

Quite symmetrically, the inverse transformation from (θ', ϕ') to (θ, ϕ) is given by

$$\begin{aligned} \cos\theta &= \cos\theta'\cos\theta_r + \sin\theta'\sin\theta_r\cos(\phi_r - \phi') \\ \sin\theta\sin(\phi - \phi_n) &= \sin\theta'\sin(\phi_r - \phi') \\ \sin\theta\cos(\phi - \phi_n) &= \cos\theta'\sin\theta_n - \sin\theta'\cos\theta_r\cos(\phi_r - \phi') \end{aligned} \tag{3}$$

Equation (3) allows us to determine the global source direction (θ_0, ϕ_0) from the local incident direction (θ_i, ϕ_i).

Finally, consider an earth-centred coordinate system defined so that the X-axis points east, the Y-axis points north and the Z-axis points vertically upwards. For a distant nadir-looking sensor, the earth-centred coordinate system and the viewer-centred coordinate system coincide, provided one aligns the viewer's X-axis with the west to east direction. For off-nadir viewing sensors, the two coordinate systems differ and one must again define transformations between the two. Fortunately, the form of the transformation and its inverse is identical to that given above. Let (θ_v, ϕ_v) be the direction to the viewer in the earth-centred coordinate system and let (θ_n, ϕ_n) now denote the vertical direction in the viewer-centred coordinate system. Let (θ, ϕ) be

any direction in the earth-centred coordinate system. Then, Equations (2) and (3) apply with subscript v replacing subscript r. Thus, one can take an arbitrary direction (θ,ϕ) given in a viewer-centred coordinate system and transform it to the corresponding direction (θ',ϕ') in the earth-centred coordinate system and vice versa. Of course, for nadir looking sensors $\theta_v = \theta_n = 0$ and $(\theta',\phi') = (\theta,\phi)$.

A digital terrain model can be thought of as a function $z = f(x,y)$ defined in the earth-centred coordinate system. The direction of a surface normal can be found by taking the cross-product of any two vectors lying in the tangent plane, provided they are not parallel to each other. Two such vectors are $[1,0,p]$ and $[0,1,q]$ where p is the slope in the west to east direction and q is the slope in the south to north direction. Thus, a surface normal is given by

$$[1,0,p] \times [0,1,q] = [-p,-q,1]$$

The quantity (p,q) is called the gradient and is another way to specify direction in the earth-centred coordinate system. A unit vector is obtained by dividing the vector $[-p,-q,1]$ by its magnitude $\sqrt{1+p^2+q^2}$. In spherical coordinates, a unit vector is given by $[\cos\phi\sin\theta,\sin\phi\sin\theta,\cos\theta]$. To find (θ,ϕ) from (p,q) one equates components of the corresponding unit vectors to obtain

$$\begin{aligned}
\cos\phi &= \frac{-p}{\sqrt{p^2+q^2}} \\
\sin\phi &= \frac{-q}{\sqrt{p^2+q^2}} \\
\cos\theta &= \frac{1}{\sqrt{1+p^2+q^2}} \\
\sin\theta &= \frac{\sqrt{p^2+q^2}}{\sqrt{1+p^2+q^2}}
\end{aligned} \tag{4}$$

Conversely,

$$\begin{aligned}
p &= -\cos\phi\tan\theta \\
q &= -\sin\phi\tan\theta
\end{aligned} \tag{5}$$

One also needs to find i, e and g from the gradient (p,q). Let the light source direction have gradient (p_0,q_0). That is, the vector $[-p_0,-q_0,1]$ points in the direction of the light source. For nadir looking sensors, the vector [0,0,1] points in the direction of the viewer. Expressing the cosine of the angle between two vectors as a normalized dot product of the vectors, one obtains

$$\begin{aligned} \cos(i) &= \frac{1 + pp_0 + qq_0}{\sqrt{1 + p^2 + q^2}\sqrt{1 + p_0^2 + q_0^2}} \\ \cos(e) &= \frac{1}{\sqrt{1 + p^2 + q^2}} \\ \cos(g) &= \frac{1}{\sqrt{1 + p_0^2 + q_0^2}} \end{aligned} \tag{6}$$

The Bidirectional Reflectance Distribution Function

The bidirectional reflectance distribution function (BRDF) was introduced by Nicodemus *et al.* (1977) as a unified notation for the specification of reflectance in terms of both the incident and the reflected beam geometry. The BRDF is an intrinsic property of the surface material and determines how bright a surface will appear when viewed from a given direction and illuminated from another. A phenomenological derivation of the BRDF is given in Appendix A. The BRDF, denoted by the symbol f_r, is the ratio of reflected radiance dL_r in the direction toward the viewer to the irradiance dE_i in the direction from a portion of the source. That is,

$$f_r(\theta_i,\phi_i;\theta_r,\phi_r) = \frac{dL_r(\theta_i,\phi_i;\theta_r,\phi_r;E_i)}{dE_i(\theta_i,\phi_i)} \qquad [\mathrm{sr}^{-1}] \tag{7}$$

Directions are given in spherical coordinates (θ,ϕ). Subscript i denotes quantities associated with the incident radiant flux and subscript r denotes quantities associated with the reflected radiant flux. (See Figure 4.)

The BRDF allows one to determine reflectance for any defined incident and reflected beam geometry simply by integrating over the specified solid angles. A systematic approach to

calculating the reflectance map has already been given (Horn & Sjoberg (1979)). Results for Lambertian surfaces and Minnaert surfaces are summarized below. The derivations for Minnaert surfaces are novel and are included in Appendix B.

Lambertian Surfaces

An ideal (lossless) diffuse surface has BRDF

$$f_r = \frac{1}{\pi} \tag{8}$$

When illuminated by a collimated source with irradiance E_0 measured perpendicular to the beam of light arriving from direction (θ_0,ϕ_0), one obtains, for points not in shadow

$$L_r = \frac{E_0}{\pi} \cos(i) \tag{9}$$

Equation 6 is used to express scene radiance as a function of surface gradient. The reflectance map becomes

$$R(p,q) = \frac{E_0}{\pi} \frac{1 + pp_0 + qq_0}{\sqrt{1 + p^2 + q^2}\sqrt{1 + p_0^2 + q_0^2}} \tag{10}$$

where (p_0,q_0) is the gradient corresponding to (θ_0,ϕ_0) determined by Equation (5). A surface with gradient (p_0,q_0) is normal to the direction of the collimated source.

When illuminated by a hemispherical uniform source with radiance L_0 over the visible hemisphere, one obtains

$$L_r = L_0 \frac{1 + \cos(e)}{2} \tag{11}$$

Here, the dependence on e arises because differing surface elements see differing amounts of sky depending on surface slope. The reflectance map becomes

$$R(p,q) = \frac{L_0}{2}\left[1 + 1/\sqrt{1 + p^2 + q^2}\right] \tag{12}$$

Minnaert Surfaces

Minnaert (1941) considered a class of surfaces with BRDF

$$f_r = \frac{k+1}{2\pi}[\cos\theta_i \cos\theta_r]^{k-1} \tag{13}$$

where, to be physically meaningful, $0 \leq k \leq 1$.

When illuminated by a collimated source with irradiance E_0 measured perpendicular to the beam of light arriving from direction (θ_0,ϕ_0), one obtains for points not in shadow

$$L_r = \frac{E_0\,(k+1)}{2\,\pi} \cos^k(i)\,\cos^{k-1}(e) \tag{14}$$

A Lambertian surface corresponds to the case $k = 1$. A scene radiance equation similar to that for scanning electron microscope (SEM) images is obtained for the case $k = 0$ (Ikeuchi & Horn (1981)). For the case $k = 1/2$ one obtains a scene radiance equation that is constant for constant $\cos(i)/\cos(e)$. This is similar to the one estiminated for the lunar surface (Minnaert (1961)), (Hapke (1971)) and for regions of Mars (Young & Collins (1971)). The reflectance map becomes

$$R(p,q) = \frac{E_0\,(k+1)}{2\,\pi}\left[\frac{1 + pp_0 + qq_0}{\sqrt{1 + p_0^2 + q_0^2}\;(1 + p^2 + q^2)}\right]^k \sqrt{1 + p^2 + q^2} \tag{15}$$

where (p_0,q_0) is the gradient corresponding to (θ_0,ϕ_0).

When illuminated by a hemispherical uniform source with radiance L_0 over the visible hemisphere, one obtains

$$L_r = L_0\cos^{k-1}(e)\left[1 - \frac{\sin^{k+1}(e)}{2\pi}\left[\frac{\Gamma(\frac{1}{2})\Gamma(\frac{k+2}{2})}{\Gamma(\frac{k+3}{2})}\;F(\tfrac{k+1}{2},\tfrac{1}{2};\tfrac{k+3}{2};\sin^2(e))\right]\right] \tag{16}$$

where $\Gamma(z)$ is the gamma function and $F(\alpha,\beta;\gamma;z)$ is the hypergeometric series as defined in Appendix B. For $k = 1$, this reduces to the Lambertian case (Equation (11)). The reflectance map again can be obtained by substitutions based on Equation (6) but is not shown here.

SCENE RADIANCE EQUATION FOR REMOTE SENSING

The atmosphere and adjacent targets complicate the scene radiance equation for remote sensing in a number of ways as illustrated in Figure 8 and as discussed below. A target, not in shadow, sees an attenuated solar beam with irradiance $E_0 T_d \cos(i)$ where E_0 is the solar irradiance at the top of the atmosphere, T_d is the downward transmission through the atmosphere and i is the angle of incidence at the target. Values of E_0 applicable to Landsat MSS and TM are given in Table 1.

A target, even when in shadow, receives diffuse sky irradiance. Components of skylight include radiation from the sun scattered by the atmosphere to the target (both single and multiple scattering), radiation reflected directly to the target from adjacent targets and radiation reflected from adjacent targets that is scattered by the atmosphere back to the target. The component of sky radiance due to adjacent targets is small in areas of low albedo but may become significant for areas of high albedo or in rugged terrain. Sky irradiance, integrated radiance over the hemisphere of the sky, is denoted by E_S.

The fraction of the total irradiance reflected in the direction of the sensor depends on the BRDF of the target. But, the reflected radiance is further attenuated by the atmosphere before it reaches the sensor. Let T_u be the upward transmission through the atmosphere.

A final complication concerns radiation reaching the sensor that does not come directly from the target. Let path radiance L_P denote all radiant energy from outside the target that reaches the sensor due to the scattering of radiation in the atmosphere. Path radiance includes radiation scattered to the sensor from the direct solar beam (both by single and multiple scattering) as well as radiation scattered to the sensor from light reflected by adjacent target areas.

Single scattering from the direct solar beam, called primary scattering, is the major component of path radiance in optically thin atmospheres. The component of path radiance due to adjacent targets is small in areas of low albedo but may become significant as the albedo of the ground increases (Otterman *et al.* (1980)). As the albedo of the ground increases, sky radiance also increases, especially near the horizon. Adjacent targets of high albedo increase both path radiance and sky irradiance at the target. These two effects are difficult to separate, especially in areas of rugged terrain (Dozier & Frew (1981)).

Extending results to atmospheres with significant multiple scattering requires a solution to the radiative transfer problem for the ambient radiation field (Turner & Spencer (1972)). This further couples all atmospheric effects together and makes it difficult to treat them separately.

Simplifying Assumptions

A full treatment of all components of the scene radiance equation is currently not feasible. Instead, a number of simplifying assumptions are made:

1. The atmosphere is assumed to be an optically thin, horizontally homogeneous layer. This reduces a three-dimensional problem to a one-dimensional problem by allowing optical depth to be defined locally as an exponential function of elevation.

2. Radiation arising from adjacent targets, including clouds, is not considered.

3. The sensor views the target from directly overhead.

4. The sky is assumed to be a uniform hemispherical source with radiance varying as an exponential function of elevation.

5. Ground cover is assumed to be Lambertian with BRDF $f_r = \rho/\pi$ where ρ is the ratio of

radiant flux reflected compared to that of an ideal (lossless) Lambertian surface.

Assumptions 1 and 2 are the most restrictive in that they allow radiometric correction to be defined as a local function of elevation and surface orientation. Relaxing 1 and 2 would necessitate analysis over extended spatial contexts. Assumption 3 simplifies the coordinate transformations required but is otherwise not restrictive. The results can easily be extended to off-nadir sensors. Assumptions 4 and 5 are straightforward to relax when better models become available. A scene radiance equation can be derived for any distribution of sky radiance and for any given BRDF.

Scene Radiance Equation

With these assumptions, the scene radiance equation, including atmospheric effects, becomes

$$L_r = T_u \frac{\rho}{\pi} \left[E_0 T_d \cos(i) + E_S \frac{(1 + \cos(e))}{2} \right] + L_P \qquad (17)$$

It remains to find expressions for T_u, T_d, E_S and L_P as functions of elevation. The upward and downward transmissions are easily derived once optical thickness is introduced as an auxiliary quantity.

Optical Thickness

The atmosphere attenuates light passing through it by absorption and scattering. One can define the volume extinction coefficient β at any point in the atmosphere to be the fraction of radiant energy removed from a light beam per unit length of travel. For a horizontally homogeneous atmosphere, the volume extinction coefficient depends only on elevation $\beta = \beta(z)$.

The optical thickness τ of an atmospheric mass measures the total extinction experienced by a light beam passing through it. The optical extinction for a vertical path from an elevation z to the top of the atmosphere is given by

$$\tau(z) = \int_z^\infty \beta(t)dt \tag{18}$$

(For the case of vertical transmission, τ is also called optical depth.) The optical thickness for a slanted path making a polar angle θ with the vertical from an elevation z to the top of the atmosphere is given by

$$\tau(z) = \int_z^\infty \frac{\beta(t)}{\cos(\theta)}dt \tag{19}$$

Optical thickness depends on the density and size distribution of particles in the atmosphere and on their scattering and absorption properties. For the visible and near infrared portion of the spectrum, three classes of particle are relevant: molecules, aerosols and ozone. Molecules of air are small with respect to the wavelength of light and contribute to Rayleigh scattering. Aerosols are particles large with respect to the wavelength of light and contribute to Mie scattering. Ozone absorbs radiation.

Based on published standard atmospheres (Valley (1965)), the Rayleigh, the Mie and the total optical thickness vary almost exponentially with elevation. Let

$$\tau(z) = \tau_0 \, e^{-z/H_\tau} \tag{20}$$

where parameter $\tau_0 = \tau(0)$ is the optical thickness at sea-level and parameter H_τ is the scale height.

The transmission between any two points in the medium depends on optical thickness according to the Lambert-Bouguer's law of transmission. The upward and downward transmissions become

$$T_u(z) = e^{-\tau(z)}$$
$$T_d(z) = e^{-\tau(z)/\cos(g)} \tag{21}$$

Sky Irradiance and Path Radiance

There have been a number of theoretical studies of radiative transfer mechanisms within the atmosphere that allow one to estimate sky radiance and path radiance. These studies assume a horizontally homogeneous atmosphere over a horizontal Lambertian surface. Results predict sky radiance and path radiance as a function of optical thickness and average background albedo. Since optical thickness depends on elevation, so do sky radiance and path radiance.

One can assume that both sky irradiance and path radiance also vary almost exponentially with elevation. Let

$$E_S(z) = E_{S0}\, e^{-z/H_S} \tag{22}$$

$$L_P(z) = L_{P0}\, e^{-z/H_P} \tag{23}$$

where parameters $E_{S0} = E_S(0)$ and $L_{P0} = L_P(0)$ are the sky irradiance and path radiance at sea-level and parameters H_S and H_P are the respective scale heights.

Scene Radiance Equation (Parametric Form)

The scene radiance equation can now be expressed as the sum of three terms. For points not in shadow

$$\begin{aligned} L_r = \quad & \frac{\rho}{\pi} E_0\, e^{-\tau(z)(1+1/\cos(g))} \cos(i) \\ & + \frac{\rho}{\pi} E_{S0}\, e^{-\tau(z)}\, e^{-z/H_S}\, \frac{(1+\cos(e))}{2} \\ & + L_{P0}\, e^{-z/H_P} \end{aligned} \tag{24}$$

where $\tau(z) = \tau_0\, e^{-z/H_\tau}$. For points in shadow, the first term for direct solar irradiance drops out but the two terms for sky irradiance and path radiance remain.

The six unknown atmospheric parameters τ_0, H_r, E_{S0}, H_S, L_{P0} and H_P remain to be estimated. Once these parameters are estimated, equation (24) can be solved for ρ to determine the albedo map.

EXPERIMENTAL RESULTS

The study site is a 21.60 km by 30.36 km area surrounding St. Mary Lake in southeastern BC, (latitude N 49 36 30, longitude W 116 11 30). The area has rugged terrain with elevations varying from 944 m to 2684 m above sea-level. Elevation data along ridges and channels was manually digitized from the 1:50,000 Canadian National Topographic System (NTS) map sheet 82 F/9 (St. Mary Lake). The ridge and channel structure was represented initially using a Triangulated Irregular Network (TIN) (Peucker *et al.*(1978)). Two grid representations were produced from the TIN. A 360 x 506 DTM (60 m grid) was used for the geometric rectification of Landsat images. Rectification was performed automatically using the method described in Little (1980). A smaller scale 180 x 253 DTM (120 m grid) was used for radiometric correction, as described below. Grid coordinates in the DTM correspond to the Universal Transverse Mercator (UTM) map projection used in Canadian NTS maps.

The exact timing of overflight for each Landsat MSS image is given in the ancillary data recorded with each scan line. The position of the sun is determined by a computer program based on the method of Horn (1978). The direction to the sun is represented as a gradient (p_0,q_0). The test site is small enough in area that (p_0,q_0) can be considered constant throughout.

The gradient (p,q) at each point in the DTM is estimated by

$$p = \frac{f(x+1,y) - f(x-1,y)}{2\Delta x} \qquad q = \frac{f(x,y+1) - f(x,y+1)}{2\Delta y} \tag{25}$$

where Δx and Δy are the DTM grid spacings expressed in the same units as $f(x,y)$. The gradient is used to determine values for $\cos(i)$ and $\cos(e)$ as required using Equation (6). The gradient is also used to generate an ancillary mask file identifying terrain points that are flat. This mask file is available to exclude flat terrain when estimating parameters related to slope and aspect.

Another mask file is generated to identify terrain points that lie in shadow. A coordinate system is erected corresponding to a viewer looking from the direction of the sun and a hidden-surface algorithm is applied to determine terrain points that are visible from that viewpoint (Woodham (1980b)). Points that are not visible are set in the shadow mask.

Estimating Path Radiance

The dependency of path radiance on elevation can be examined by plotting measured scene radiance as a function of elevation. Plots typically show that the minimum recorded radiance is a decreasing function of elevation (Woodham (1980b)), (Sjoberg (1982)). If ground cover of zero albedo occurs at all elevations, then the sea-level value and scale height for path radiance can be estimated from the minimum recorded scene radiances.

The estimation problem is linearized by taking the logarithm of equation (23) to obtain

$$\ln\left(L_P(z)\right) = \ln\left(L_{P0}\right) - \frac{1}{Hp}\, z \tag{26}$$

A least squares estimate won't do, however, since we need the best-fit straight line falling under the logarithm of the minimum radiances. Instead, the problem is translated into a linear programming problem and solved by the simplex method. Let r_i be the logarithm of the minimum radiance at elevation z_i. Let $A = 1/Hp$ and $B = \ln\left(L_{P0}\right)$. Then, the problem is

$$\begin{aligned} \text{minimize} \quad & \sum_{i=1}^{n} (r_i - B + A\ z_i) \\ \text{where} \quad & r_i - B + A\ z_i \geq 0, \quad i = 1,\ldots,n \\ & A\,, B \geq 0 \end{aligned} \tag{27}$$

which, on further manipulation, becomes

$$\begin{aligned} \text{maximize} \quad & nB - A \sum_{i=1}^{n} z_i \\ \text{where} \quad & B - A\, z_i \leq r_i, \quad i = 1,\ldots,n \\ & A, B \geq 0 \end{aligned} \tag{28}$$

Table 2 includes the estimated values for L_{P0} and H_P. Two cautions are in order. First, elevations in the St. Mary Lake area vary from 944 m to 2684 m. Extrapolation outside of this range is difficult. Second, sky irradiance also decreases with increasing elevation. Without targets of near zero albedo, components of sky irradiance will be included causing an overestimate of path radiance (Ahern *et al.* (1977)).

Estimating Sky Irradiance and Optical Thickness

After correcting for path radiance $L_P(z)$, the scene radiance equation becomes

$$\begin{aligned} L_r - L_P(z) = \quad & \frac{\rho}{\pi} E_0\, e^{-\tau(z)(1+1/\cos(g))} \cos(i) \\ & + \frac{\rho}{\pi} E_{S0}\, e^{-\tau(z)}\, e^{-z/H_S}\, \frac{(1+\cos(e))}{2} \end{aligned} \tag{29}$$

where $\tau(z) = \tau_0 e^{-z/H_\tau}$. Three methods are used to estimate E_{S0}, H_S, τ_0 and H_τ.

Method I simply applies results available from other sources. Ideally, one would like to take advantage of field measurements obtained at the time of satellite overflight. For this study, independent measurements of sky irradiance and optical depth were not available so Method I used results obtained from the literature. For example, we follow Sjoberg (1982) who estimated optical thickness by fitting an exponential to the data for the U.S. Standard Atmosphere (Valley (1965)), selected a suitable value for E_{S0} and set $H_S = H_P$.

Method II uses cast shadow boundaries to estimate the required parameters. The idea is illustrated in Figure 9. Shadow boundaries are traversed in the direction from the sun azimuth. Shadow boundary points corresponding to transitions from light to dark typically correspond to terrain breaks and are not used. Points on cast shadow boundaries corresponding to transitions

from dark to light vary with the position of the sun. One can therefore assume that the ground cover across a cast shadow boundary remains constant, provided that we exclude cast shadow points that happen also to coincide with terrain breaks. Further, one can assume that sky irradiance and optical thickness are locally constant across cast shadow boundaries. Taking the ratio of the path radiance corrected measurement on the shadow side to the difference between the sunlit side and the shadowed side, one obtains

$$\frac{L_{r\ (shadow)} - L_P(z)}{L_{r\ (sun)} - L_{r\ (shadow)}} = \frac{E_{S0}\, e^{-z/H_S}\, (1 + \cos(e))}{2\, e^{-\tau(z)/\cos(g)}\, E_0 \cos(i)} \tag{30}$$

Values for $\cos(i)$, $\cos(e)$, $\cos(g)$ and z are known locally. Estimates are obtained for τ_0, H_r, E_{S0} and H_S from Equation (30) using a non-linear curve fitting algorithm.

Method III makes use of ground cover of known albedo lying in shadow. In winter most areas are covered by snow. In particular, it is safe to assume that the lake itself and all elevations above 2300 m are snow covered. The albedo of snow is set to a constant, in this case $\rho = 0.95$ for band 4, and the scene radiance equation for points in shadow becomes

$$L_{r\ (shadow)} - L_P(z) = \frac{0.95}{\pi}\, E_{S0}\, e^{-\tau(z)}\, e^{-z/H_S}\, \frac{(1 + \cos(e))}{2} \tag{31}$$

Values for $\cos(e)$ and z are known locally. Estimates for τ_0, H_r, E_{S0} and H_S are obtained from Equation (31) using a non-linear curve fitting algorithm.

Generation of the Albedo Map

Method I was applied to both the January 8, 1979 and the September 17, 1979 images. Methods II and III were applied only to the January image owing to the absence of significant shadow in the September image. The estimates for the six atmospheric parameters are given in Table 2. Table 2(a) lists values estimated for L_{P0}, H_P, E_{S0}, H_S, τ_0 and H_r. Table 2(b) lists values for $L_P(z)$, $E_S(z)$ and $\tau(z)$ confined to the range of elevations, 944 m to 2684 m, that

actually occur in the test site.

Given a set of parameter estimates, the albedo map is generated by solving the scene radiance equation for ρ. Figure 10 repeats the example of Figure 1 but with the sun at an elevation of 13.8 degrees and an azimuth of 153.1 degrees corresponding to its true position over St. Mary Lake at 19:58 GMT on January 8, 1979. Figure 11 presents the albedo map determined by method III applied to band 4 of the January image. About 43.2% of the test area lies in shadow.

OTHER APPLICATIONS

Automatic Hill Shading

Hill shading is one way to depict surface form on maps. Hill shading is useful because it provides for quick comprehension of topography. Hill shading appeals to the human perceiver's ability to relate differences in brightness to differences in surface shape. Hill shading has been used for many centuries, the methods varying according to the technology of the day. A comprehensive review of hill shading techniques, using the reflectance map as a unifying representation, has been given by Horn (1981).

Synthetic image generation is a form of automatic hill shading. In image analysis, we use a synthetic image to predict, as closely as possible, the actual measurements obtained from image sensors. Many of the factors considered, such as shadows, sky radiance and atmospheric attenuation, detract from the cartographic rendering of terrain and are not included in automatic hill shading. Even so, automatic methods based on a fixed light source distribution and a fixed BRDF are considered inferior to the best manual methods.

One reason is that contrast is often lost across terrain features that lie in the direction of sun azimuth. A comparison of Figure 2(a) and 2(b) reveals that some terrain features are more clearly defined in one image than in the other, and vice versa. One interpretation of the cartographer's craft in manual hill shading is to adjust the position of the light source locally to provide the best rendering of the terrain. Humans appear not to notice that the effective light source position varies from place to place. Automatic hill shading of this sort would require sophisticated local terrain analysis.

Two contributions to automatic hill shading follow from the methods described. First, multiple synthetic images can be combined into a single image using colour. The cartographic convention for hill shading is to place the light source in the north-west at an elevation of 45

degrees. A second image is generated with the light source in the north-east at an elevation of 45 degrees. A colour composite is produced by assigning different colours to the two images, say blue for the first and green for the second. This rendering provides an unambiguous representation of slope and aspect. It is also useful to encode elevation directly in a third colour, say red. The result is easy to interpret and provides an effective portrayal of surface form.

Second, automatic hill shading based on a fixed light source and a fixed BRDF has been extended to allow the position of the light source to be varied interactively. The image frame buffer contains quantized values of the gradient (p, q). For a given light source distribution, the reflectance map $R(p, q)$ is calculated at each quantized value of (p, q) and the result is represented as a lookup table. Moving the light source requires only that the lookup table be recomputed. Realtime performance is achieved since this computation can proceed at video rates. Jankowski (1984) developed gradient quantization techniques to exploit this idea. No degradation in image quality occurs, provided a frame buffer with a least 12 bits/pixel is available to represent the surface gradient.

Synthesizing Oblique Views

Once an image has been registered to a DTM, it is possible to further transform the image to simulate alternate viewpoints (Tanaka & Suga (1979)). In the current context, the geometric transformation required follows immediately from the method used for shadow determination. With the viewer looking from an arbitrary "sun" direction (p_0, q_0), the hidden-surface algorithm is again applied. The transformation that determines whether a point is visible also determines the position of that point in a viewer-centred coordinate system aligned with the sun direction. Mapping image brightness values directly to this new coordinate system produces an oblique view as illustrated in Figure 12.

For what class of surface materials is this transformation justified? Ignoring the question of differing atmospheric path length, the transformation is correct only for Lambertian surfaces. (Lambertian surfaces are the unique class of surfaces for which brightness from one viewpoint equals brightness from all viewpoints.) If the BRDF of the surface material $f_r(\theta_i,\phi_i;\theta_r,\phi_r)$ depends on (θ_r,ϕ_r) then radiometric correction must be included as part of the geometric transformation.

Synthesizing Stereo Pairs

Another useful way to combine an image and a DTM is to generate a synthetic stereo pair (Batson *et al.*(1976)). Figure 13 illustrates. On a colour image display, it is possible to present the stereo pair anaglyphically. The left image is shown in cyan (blue + green) and the right image in red. When viewed through goggles with matching filters, the result is perceived as a single black and white image in stereo.

The left and right images of Figure 13 are synthesized oblique views, as described above, obtained from two nearly vertical viewpoints. The angle of convergence between viewpoints controls the degree of vertical exaggeration in the stereo presentation. The ability to view synthetic Landsat stereo pairs has facilitated the production and editing of DTM's and the verification of automatic image rectification software.

DISCUSSION

Geometric Considerations

Table 3 lists values of relief displacement applicable to the Landsat, SPOT and Seasat satellite sensors. Relief displacement was negligible for Landsat 1, 2 and 3. Thus, geometric rectification proceeded without regard to local changes in elevation. But, relief displacement is significant for Seasat (SAR) and will be significant for SPOT in off-nadir mode, even for relatively flat terrain. In rugged terrain, relief displacement is significant for Landsat TM and for SPOT in nadir mode. Rectifying multiple data sets to a common datum will require relief displacement correction. This is possible when an appropriate digital terrain model is available. Recent work uses DTM's for relief displacement correction in a high throughput system for the geometric rectification of satellite images (Wong (1984)).

Often, one considers geometric and radiometric correction independently. This works well for nadir looking sensors, such as Landsat, because negligible error is introduced by geometric preprocessing that, in effect, presumes all targets are seen from the vertical and through the same atmosphere. Thus, radiometric correction, as described here, can be applied after the image has been geometrically rectified.

Independence cannot be presumed for off-nadir sensors, such as Seasat and SPOT. Algorithms for radiometric correction require the local incident and reflected beam geometry at the time of target acquisition. This is certainly required to correct for differing slant path atmospheric thickness. To the extent that natural surfaces are not Lambertian, this is also required to adjust for the change in (θ_r, ϕ_r) from actual to rectified sensor position.

For terrain of a given roughness, the maximum angle θ_r that occurs during imaging increases as the sensor becomes increasingly off-nadir. Thus, any dependence of the BRDF of

the surface on θ_r becomes increasingly important to include in radiometric correction. This local information is lost if radiometric correction occurs only after geometric rectification.

Finally, local measurements across cast shadow boundaries, as used in Method II, are corrupted if the resampling used for geometric rectification has smoothly interpolated across the brightness discontinuity introduced at a shadow boundary. The measurements required to estimate atmospheric parameters are best made prior to geometric rectification and should, in fact, influence the resampling procedure used for geometric rectification. Ideally, geometric rectification should resample based on intrinsic scene properties, such as albedo. For off-nadir sensors, interpolating scene radiance directly is only a crude approximation to this ideal.

The Lambertian Assumption

The assumption that natural surfaces behave like Lambertian reflectors has been investigated in the literature. (Justice *et al.* (1980) provides a survey.) One approach has been to apply a correction based on $\cos(i)$ and to subjectively evaluate the result. One assumes scene radiance is given by

$$L_r = a\ \rho \cos(i) + b \tag{32}$$

where a and b are constants and ρ is the albedo. Constants a and b are estimated by a linear regression of L_r and $\cos(i)$, assuming some average value for ρ. The corrected albedo map is then produced by solving Equation (32) locally for ρ. That is,

$$\rho = \frac{L_r - b}{a\ \cos(i)} \tag{33}$$

This method has been found to overcorrect in areas of steep terrain, particularly in the shorter wavelength bands. This subjective observation is supported by a more objective measure. That is, correction based on this method does not lead to improved map accuracy in spectral classification.

In retrospect, this result should not be surprising. Sky irradiance is significant and cannot be ignored, particularly in the shorter wavelength bands. Steep terrain tends also to correspond to terrain approaching the grazing angle of incident solar radiation. Here, sky irradiance dominates and any method that does not explicitly take it into account will necessarily overcorrect. Sky irradiance varies with elevation and slope and cannot be absorbed into the constant b. Thus, this correction method would fail with the same symptoms even if the surface were Lambertian.

Another approach has been to consider Minnaert surfaces and to estimate an appropriate value of the free parameter k (Smith *et al.* (1980)), (Teillet *et al.* (1982)). Here, one assumes scene radiance is given by

$$L_r = a\ \rho \cos^k(i)\cos^{k-1}(e) \tag{34}$$

where a is a constant and ρ is the albedo. Equation (34) can be linearized by first multiplying each side by $\cos(e)$ and then taking the logarithm. One obtains,

$$\ln(L_r\ \cos(e)) = k\ \ln(\cos(i)\cos(e)) + \ln(a\ \rho) \tag{35}$$

The value of k is estimated by a linear regression of $\ln(L_r\ \cos(e))$ and $\ln(\cos(i)\cos(e))$. An albedo map is then produced as before.

This method was applied to the January 8, 1979 and September 17, 1979 images presented above. A third image from September 25, 1974 (frame-id 10794-17572) is included for comparison purposes. The estimates of k for each Landsat band are presented in Table 4. The results for the two September images agree with those presented in Teillet *et al.* (1982). This is to be expected since the test sites are geographically similar and the images are obtained at roughly the same time of year.

The results suggest that, over the class of Minnaert surfaces, a Lambertian model is adequate for band 7 but inadequate for bands 4 and 5. But, this approach has the same deficiency

as before. That is, Equation (34) applies only to a Minnaert surface illuminated by a collimated source (i.e., the sun). Under a hemispherical uniform source one formally obtains something quite different (recall Equation (16)). It is unrealistic to assume that sky irradiance is adequately captured by the parameter k. In particular, the results for the January image show statistical estimates of k all greater than 1.0. This is inconsistent with the physical requirement that $0 \leq k \leq 1$.

Spectral Considerations

Of course, reflectance is also dependent on the wavelength λ of the radiation. Selective reflection frequently alters the spectral distribution of the reflected beam. If there is interaction between spectral and geometric factors, as can be the case for materials with significant internal scattering, the geometric distribution is also affected. On the other hand, if there is no interaction between wavelength and the geometric dependence of reflection then

$$f_r(\theta_i,\phi_i;\theta_r,\phi_r;\lambda) = f_r(\theta_i,\phi_i;\theta_r,\phi_r)\, f_r(\lambda) \tag{36}$$

where $f_r(\theta_i,\phi_i;\theta_r,\phi_r;\lambda)$ is the spectral bidirectional reflectance distribution function and $f_r(\lambda)$ is a weighting function that determines relative reflection as a function of λ. If equation (36) holds, the function $f_r(\theta_i,\phi_i;\theta_r,\phi_r;\lambda)$ is said to be separable.

Unfortunately, there is no data that will establish the extent to which there is interaction between geometric dependence and spectral dependence in remote sensing applications. Intuition based on terrestrial observations would suggest that the spectral BRDF of most natural surfaces is, to a first approximation, separable, at least over the wavelength bands in the visible portion of the spectrum. Suppose a material was non-separable in the sense of equation (36). Then there would be change in the spectral distribution of scene radiance as a function the incident direction and the viewing direction. There are few objects whose perceived colour changes with movement as non-separability would suggest. One must be cautious, however,

about relying on such intuitions. They may say more about the robustness of human colour perception than about intrinsic characteristics of surface materials.

The BRDF of a Minnaert surface is not separable when k depends on λ. Consider a Minnaert surface viewed the two configurations shown in Figure 14. Suppose that red, green and blue bands are obtained and that the corresponding known values of k are 1.0, 0.5 and 0.25. Suppose $\theta = \pi/8$. The normalized components of red, green and blue are (.539,.584,.607) for Figure 14(a) and (.341,.574,.744) for Figure 14(b). This represents a significant shift towards the blue for a rotation of only 45 degrees about the point of observation.

If the above colour values were obtained from remote sensing measurements of an unknown surface then there are at least two possible explanations. One is that the surface is indeed of the Minnaert class with values of k that depend on λ. The other is that there are additional components of source radiance that must be considered. The example of Figure 14 only considers a collimated source. Diffuse background radiance adds complication, especially if the spectral distribution of the background radiance differs from that of the collimated source.

Atmospheric Considerations

The six parameters introduced to model the atmosphere are tightly coupled together and difficult to treat independently. Without extended targets of near zero albedo, it is difficult to separate path radiance from sky irradiance. Without shadow regions over the full range of elevations, Methods II and III have trouble estimating the dependence of sky irradiance and optical thickness on elevation. Without better models of the local dependence of sky irradiance on surface slope and adjacent terrain, it is difficult to separate optical thickness from sky irradiance. On the other hand, substantial trade-off between these six parameters can occur while still producing similar albedo maps.

Shadows are important in rugged terrain. An earlier paper pointed out that ground cover of high albedo in shadow can be brighter than adjacent ground cover of low albedo in direct sunlight (Woodham (1980b)). This suggests that sky radiance can neither be ignored nor implicitly absorbed into other parameters of the scene radiance equation. Here, sky radiance has been explicitly modeled as a hemispherical uniform source with radiance depending on elevation.

The spatial distribution of sky radiance is not strictly uniform, even under clear sky conditions (Steven (1977)), (Kirchner *et al.* (1982)). Partly cloudy conditions produce even more complex distributions. Measurements of sky radiance typically show brightening near the horizon indicating that adjacent terrain is important (Stewart (1984)). An exciting possibility is to develop site specific models of sky radiance and to integrate them into a scene radiance equation applicable to images acquired over that site.

Evaluation

Sjoberg (1982) estimated the required six atmospheric parameters using a global least squares estimator applied to a linearized version of the problem. This proved unsatisfactory in part because the method was extremely sensitive to required initial assumptions about the surface albedo. Considerable success was achieved, nevertheless, by trial and error experimentation with different parameter estimates. The methods described in this paper extend these ideas to automatically estimate the required six parameters using local measurements in shadow regions. The results suggest that radiometric correction can be applied to images acquired under a wide variety of terrain and imaging conditions.

But, formal evaluation criteria need to be developed. The only obvious criterion is that albedo must lie between zero and one. The methods described generally achieve this except along seams of slight shadow miss-registration or along sharp ridges that have been smoothed in

the DTM. Another criterion would be consistency in albedo estimation over time. Unfortunately, albedo depends on many factors, including some like surface moisture that vary rapidly over the time period between successive Landsat overflights. It would be useful to test these methods on images acquired at different times on the same day. A true evaluation, however, will require methods to estimate atmospheric parameters that don't rely quite so heavily on shadow regions.

In the current investigation, evaluation criteria are primarily subjective. One looks to see if shadows are removed, if known homogeneous areas appear homogeneous independent of slope and aspect and if atmospheric corrections are appropriate over the full range of elevations that occur in the scene.

CONCLUSIONS

Conclusions following from this investigation are summarized below:

1. Atmospheric effects are important and vary locally with elevation, particularly in the shorter wavelength bands.

2. Sky irradiance is significant and must be dealt with explicitly. Further work is required to develop adequate models of sky radiance.

3. Shadow regions are useful because they provide a local context to estimate sky irradiance.

4. Parameters used to model scene radiance are best derived from physical considerations. Physical models correctly characterize simple worlds and can be elaborated as the need is demonstrated.

5. The rejection of the Lambertian assumption is premature. There is no compelling evidence to reject the assumption that the spectral BRDF of most natural surfaces is separable. Experiments that show values of k close to 1 for measurements of Landsat MSS band 7 suggest that the Lambertian assumption is the right one over the class of Minnaert surfaces considered, especially since atmospheric effects are minimized for this band.

ACKNOWLEDGEMENT

Tom Poiker of Simon Fraser University provided original software for the representation and manipulation of digital terrain models. Digitization of NTS mapsheet 82 F/9 was done by Jim Little using the IGDS system of the Inventory Branch of the BC Ministry of Forests. Many students have contributed to implementations of the image analysis software used in this paper. The authors acknowledge the work of Stewart Kingdon, Jim Little, Mike Palmer and Robert Redekop. Figure 12 was prepared by Jim Little. Figure 13 was prepared by Stewart Kingdon. All drawings are by Nedenia M. Holm. May Vink assisted in the preparation of the manuscript.

This report describes research done at the Laboratory for Computational Vision of the University of British Columbia. Support for the laboratory's remote sensing research is provided by the UBC Interdisciplinary Graduate Program in Remote Sensing, by the Natural Sciences and Engineering Research Council of Canada (NSERC) under grants A3390, A0383 and SMI-51 and in by the Canadian Institute for Advanced Research. Acquisition of the Landsat data used in this study was funded by a grant from the BC Ministry of Forests.

REFERENCES

(1) Ahern, F.J., D.G. Goodenough, S.C Jain, V.R. Rao & G. Rochon (1977), "Use of Clear Lakes as Standard Reflectors for Atmospheric Measurements", *Proc. 11th Int. Symp. on Remote Sensing of Environment,* pp 731-755.

(2) Ahern, F.J. & J. Murphy (1978), "Radiometric Calibration and Correction of Landsat 1, 2, and 3 MSS Data", Research Report 78-4, Canada Centre for Remote Sensing, Ottawa, Ont.

(3) Batson, R.M., K. Edwards & E.M. Eliason (1976), "Synthetic Stereo and Landsat Pictures", *Photogrammetric Engineering and Remote Sensing* (42)1279-1284.

(4) Dozier, J. & J. Frew (1981), "Atmospheric Corrections to Satellite Radiometric Data over Rugged Terrain", *Remote Sensing of Environment* (11)191-205.

(5) Eliason, P.T., L.A. Soderblom & P.S. Chavez, Jr. (1981), "Extraction of Topographic and Spectral Albedo Information from Multispectral Images" *Photogrammetric Engineering and Remote Sensing* (48)1571-1579.

(6) Gradshteyn, I.S & I.M. Ryzhik (1965), *Table of Integrals, Series and Products,* Academic Press.

(7) Hapke, B. (1971), "Optical Properties of the Lunar Surface", in *Physics and Astronomy of the Moon (2nd edition),* Z. Kopal (ed.) pp. 155-211, Academic Press.

(8) Haralick, R.M. & S. Wang (1983), "Relative Elevation Determination from Landsat Imagery" *Proc. 27th IEEE Computer Society Int. Conf.,* pp 284-292, Arlington, VA. (Sept. 25-29, 1983).

(9) Horn, B.K.P. (1975), "Obtaining Shape from Shading Information", in *The Psychology of Computer Vision,* P.H. Winston (ed.) pp. 115-155, McGraw-Hill.

(10) Horn, B.K.P. (1977), "Understanding Image Intensities", *Artificial Intelligence* (8)201-231.

(11) Horn, B.K.P. (1978), "The Position of the Sun", AI-WP-162, Artificial Intelligence Laboratory, MIT, Cambridge, MA.

(12) Horn, B.K.P. & R.W. Sjoberg (1979), "Calculating the Reflectance Map", *Applied Optics* (18)1770-1779.

(13) Horn, B.K.P. (1981), "Hill-shading and the Reflectance Map", *Proc. IEEE* (69)14-47.

(14) Horn, B.K.P. & K. Ikeuchi (1984), "The Mechanical Manipulation of Randomly Oriented Parts", *Scientific American* 251(2)100-111.

(15) Ikeuchi, K. & B.K.P. Horn (1981), "Numerical Shape from Shading and Occluding Boundaries", *Artificial Intelligence* (17)141-184.

(16) Jankowski, R. (1984), "Displaying Human Visual Field Data as Shaded Surfaces", M.A.Sc. Thesis, Dept. Electrical Engineering, UBC, Vancouver, BC.

(17) Justice, C.O., S.W. Wharton & B.N. Holben (1980), "Application of Digital Terrain Data to Quantify and Reduce the Topographic Effect on Landsat Data", NASA TM 81988, Goddard Space Flight Center, Greenbelt, Maryland.

(18) Kirchner, J.A., S. Youkhana & J.A. Smith (1982), "Influence of Sky Radiance Distribution on the Ratio Technique for Estimating Bidirectional Reflectance", *Photogrammetric Engineering and Remote Sensing* (48)955-959.

(19) Little, J.J. (1980), "Automatic Registration of Landsat Images Using Features Selected from Digital Terrain Models", *Proc. 3rd Can. Soc. Computational Studies of Intelligence Conf.*, pp 188-195, Victoria, BC. (May 14-16, 1980)

(20) Minnaert, M. (1941), "The Reciprocity Principle in Lunar Photometry", *Astrophys. J.* (93)403-410

(21) Minnaert, M. (1961), "Photometry of the Moon", in *The Solar System Vol. III: Planets and Satellites,* G.P. Kuiper & B.M. Middlehurst (eds.), pp. 213-248, Univ. Chicago Press.

(22) Nicodemus, F.E., J.C. Richmond, J.J. Hsia, I.W. Ginsburg & T. Limperis (1977), "Geometrical Considerations and Nomenclature for Reflectance", *NBS Monograph 160,* National Bureau of Standards, Washington, D.C.

(23) Otterman, J., S. Ungar, Y. Kaufman & M. Podolak (1980), "Atmospheric Effects on Radiometric Imaging from Satellite under Low Optical Thickness Conditions", *Remote Sensing of Environment* (9)115-129.

(24) Peucker, T.K. , R.J. Fowler, J.J. Little & D.M. Mark (1978), "The Triangulated Irregular Network", *Proc. of the Digital Terrain Models Symp.*, American Society of Photogrammetry, pp. 516-532, St. Louis, May 9-11, 1978.

(25) Robinove, C.J. (1982), "Computation with Physical Values from Landsat Digital Data", *Photogrammetric Engineering and Remote Sensing* (48)781-784.

(26) Shibata, T., W. Frei & M. Sutton (1981), "Digital Correction of Solar Illumination and Viewing Angle Artifacts in Remotely Sensed Images", *Proc. 1981 Machine Processing of Remotely Sensed Data Symposium* pp. 169-177, West Lafayette, Indiana.

(27) Sjoberg, R.W. (1982), "Atmospheric Effects in Satellite Imaging of Mountainous Terrain", AI-TR-688, Artificial Intelligence Laboratory, MIT, Cambridge, MA.

(28) Smith, J.A., T.L. Lin & K.J. Ranson (1980), "The Lambertian Assumption and Landsat Data", *Photogrammetric Engineering and Remote Sensing* (46)1183-1189.

(29) Steven, M.D. (1977), "Standard Distributions of Clear Sky Radiance", *Quarterly Journal of the Royal Meteorological Society* (106)57-61.

(30) Stewart, K.E. (1984), "The Angular Distribution of Diffuse Solar Radiation over the Sky Hemisphere", M.Sc. Thesis, Dept. of Geography, University of British Columbia, Vancouver, B.C.

(31) Tanaka, S. & Y. Suga (1979), "Landscape Drawing from Landsat MSS Data", *Photogrammetric Engineering and Remote Sensing* (45)1345-1351.

(32) Teillet, P.M., B. Guindon & D.G. Goodenough (1982), "On the Slope-Aspect Correction of Multispectral Scanner Data", *Canadian Journal of Remote Sensing* (8)84-106.

(33) Thekaekara M.P. (1970), "Proposed Standard Values of the Solar Constant and Solar Spectrum" *Journal of Environmental Sciences* (13)6-9.

(34) Turner, R.E. & M.M. Spencer (1972), "Atmospheric Model for Correction of Spacecraft Data", *Proc. 2nd International Symposium on Remote Sensing of Environment,* pp. 895-934.

(35) Valley, S.L. (ed.) (1965), *Handbook of Geophysics and Space Environments,* McGraw-Hill.

(36) Wong, F. (1984), "A Unified Approach to the Geometric Rectification of Remotely Sensed Imagery", Computer Science TR-84-6, University of British Columbia, Vancouver, BC, May, 1984.

(37) Woodham, R.J. (1978), "Reflectance Map Techniques for Analyzing Surface Defects in Metal Castings", AI-TR-457, Artificial Intelligence Laboratory, MIT, Cambridge, MA.

(38) Woodham, R.J. (1980a), "Photometric Method for Determining Surface Orientation from Multiple Images", *Optical Engineering* (19)139-144.

(39) Woodham, R.J. (1980b), "Using Digital Terrain Data to Model Image Formation in Remote Sensing", *Proc. SPIE* (238)361-369.

(40) Woodham, R.J. (1981), "Analysing Images of Curved Surfaces", *Artificial Intelligence* (17)117-140.

(41) Young, A.T. & S.A. Collins (1971), "Photometric Properties of the Mariner Cameras and of Selected Regions of Mars", *J. of Geophysical Research* (76)432-437.

APPENDIX A: THE BRDF (A PHENOMENOLOGICAL DERIVATION)

Consider a large, opaque hemisphere with walls and base that do not transmit, emit or reflect any radiation. (See Figure 15.) An infinitessimal element of an opaque reflecting material dA is placed at the centre of the base in the plane of the base. Outside the hemisphere, there is a field of radiant energy flowing in all directions. We assume, however, that the hemisphere is sufficiently large that when an infinitessimal hole subtending a solid angle $d\omega_i$ (relative to dA) is cut in the hemispherical wall only radially directed rays of radiance L_i [$W \cdot m^{-2} \cdot sr^{-1}$] can reach dA. All other rays from outside the hemisphere strike the base or walls of the hemisphere and are absorbed. No restriction is placed on the incident radiance L_i which may vary with direction. The directional dependence of L_i is denoted as $L_i(\theta_i, \phi_i)$.

Now, the incident beam strikes dA with an irradiance

$$\begin{aligned} dE_i(\theta_i,\phi_i) &= L_i(\theta_i,\phi_i)\, d\Omega_i \qquad [W \cdot m^{-2}] \\ &= L_i(\theta_i,\phi_i)\cos\theta_i \; d\omega_i \\ &= L_i(\theta_i,\phi_i)\cos\theta_i \sin\theta_i \; d\theta_i\, d\phi_i \end{aligned} \tag{37}$$

(Note: ω and Ω denote solid angle and projected solid angle respectively. The relationship $d\Omega = \cos\theta \, d\omega = \cos\theta \sin\theta \, d\theta d\phi$ holds throughout.) The incident flux (or power) reaching dA is then

$$\begin{aligned} d\Phi_i &= dE_i(\theta_i,\phi_i)\, dA \qquad [W] \\ &= L_i(\theta_i,\phi_i)\, dA \cos\theta_i \sin\theta_i \; d\theta_i\, d\phi_i \end{aligned} \tag{38}$$

In general, some of the incident flux $d\Phi_i$ is absorbed by the material and some of it is reflected into all directions within the hemisphere. In remote sensing, one cannot measure all this reflected radiation but only that portion reflected into the solid angle subtended by the sensor at the time of image acquisition. Consider an infinitessimal solid angle $d\omega_r$ in the direction (θ_r, ϕ_r) determined by cutting another hole in the hemispherical wall where the sensor is positioned. The sensor only responds to radiation reflected from dA in the direction (θ_r, ϕ_r).

The reflected radiant flux reaching the sensor through the element of solid angle $d\omega_r$ is

$$\begin{aligned} d\Phi_r &= dM_r(\theta_r,\phi_r)\, dA \qquad [\mathrm{W}] \\ &= dL_r(\theta_r,\phi_r)\, d\Omega_r\, dA \\ &= dL_r(\theta_r,\phi_r)\cos\theta_r\, d\omega_r\, dA \\ &= dL_r(\theta_r,\phi_r)\cos\theta_r \sin\theta_r\, d\theta_r\, d\phi_r\, dA \end{aligned} \tag{39}$$

where $dM_r(\theta_r,\phi_r) = dL_r(\theta_r,\phi_r)\, d\Omega_r$ is called the radiant exitance of the surface and, like $dE_i(\theta_i,\phi_i)$, it is a directional quantity.

One might consider defining a reflectance function as the ratio $d\Phi_r / d\Phi_i$. Unfortunately, this definition has an undesirable property since changing the $d\Omega_r$ subtended at the sensor produces a proportional change in $d\Phi_r$. Instead, the invariant reflectance property for the element of reflecting surface dA is the bidirectional reflectance distribution function f_r defined by

$$\begin{aligned} f_r(\theta_i,\phi_i;\theta_r,\phi_r) &= \frac{d\Phi_r}{d\Phi_r\, d\Omega_r} \qquad [\mathrm{sr}^{-1}] \\ &= \frac{dL_r(\theta_i,\phi_i;\theta_r,\phi_r;E_i)}{dE_i(\theta_i,\phi_i)} \end{aligned} \tag{40}$$

The BRDF, as defined here, is not affected by small changes in the geometry of the incident or the reflected beams, as long as they are still elements in essentially the single directions indicated. The BRDF also is not affected by changes in the strength of the incident radiation.

Finally, by Helmholtz reciprocity, which holds in the absence of polarization and magnetic fields, the directions of incident and reflected radiation can be interchanged. That is, for any BDRF f_r

$$f_r(\theta_1,\phi_1;\theta_2,\phi_2) = f_r(\theta_2,\phi_2;\theta_1,\phi_1) \tag{41}$$

Reciprocity can be used to prove, for example, that the only BRDF that is independent of viewer position (θ_r,ϕ_r) is $f_r = k$ where k is a constant. That is, it is the BRDF of a Lambertian surface.

APPENDIX B: SCENE RADIANCE FOR MINNAERT SURFACES

The BRDF of a Minnaert surface is

$$f_r(\theta_i,\phi_i;\theta_r,\phi_r) = \frac{k+1}{2\pi}[\cos\theta_i \cos\theta_r]^{k-1} \tag{42}$$

where $0 \leq k \leq 1$. It follows from the definition of the BRDF that scene radiance can be written as the integral

$$\begin{aligned} L_r(\theta_n,\phi_n) &= \int_{\Omega_i} f_r L_i \, d\Omega_i \\ &= \int_{\omega_i} f_r L_i \cos\theta_i \, d\omega_i \\ &= \int_{-\pi}^{\pi} \int_{0}^{\pi/2} f_r(\theta_i,\phi_i;\theta_r,\phi_r) \, L_i(\theta_s,\phi_s) \cos\theta_i \sin\theta_i \, d\theta_i \, d\phi_i \end{aligned} \tag{43}$$

where $L_i(\theta_s,\phi_s)$ is the source distribution given in terms of viewer-centred coordinates (θ_s,ϕ_s). The integral is defined over all incident directions in the hemisphere visible from the surface. For each incident direction, the corresponding source direction (θ_s,ϕ_s) is calculated from the surface normal (θ_n,ϕ_n) and the incident direction (θ_i,ϕ_i). Scene radiance L_r is then given as a function of surface orientation. Here (θ_n,ϕ_n) represents surface orientation.

We now derive the required expressions for scene radiance L_r first for a collimated source and then for a uniform hemispherical source.

A collimated source arriving from direction (θ_0,ϕ_0) with irradiance E_0 measured perpendicular to the beam of light is described by,

$$L_i(\theta_s,\phi_s) = \frac{E_0 \, \delta(\theta_s - \theta_0) \, \delta(\phi_s - \phi_0)}{\sin\theta_0} \tag{44}$$

where $\delta(x)$ is the Dirac delta function. Substituting this into the integral for scene radiance and recalling that $\theta_n = \theta_r$, we obtain

$$L_r = \frac{E_0(k+1)}{2\pi}\cos^{k-1}\theta_n \int_{-\pi}^{\pi}\int_{0}^{\frac{\pi}{2}} \frac{\cos^k\theta_i\,\delta(\theta_e-\theta_0)\,\delta(\phi_e-\phi_0)\sin\theta_i}{\sin\theta_0}\,d\theta_i\,d\phi_i$$

$$= \frac{E_0(k+1)}{2\pi}\cos^{k-1}\theta_n \quad \max[0,\cos^k\theta_i'] \tag{45}$$

where θ_i' is the value of θ_i corresponding to $(\theta_e,\phi_e) = (\theta_0,\phi_0)$.

A hemispherical uniform source is described by

$$\begin{aligned} L_i(\theta_e,\phi_e) &= L_0 \qquad \text{for} \quad \theta_e < \pi/2 \\ L_i(\theta_e,\phi_e) &= 0 \qquad \text{for} \quad \theta_e \geq \pi/2 \end{aligned} \tag{46}$$

Not all surface elements will see the same amount of the hemispherical source. We need to determine the value of the incident angle θ_i' that corresponds to the horizon cutoff of the source ($\theta_e = \pi/2$). From the coordinate transformation equations, one obtains

$$\cot\theta_i' = -\tan\theta_r\cos(\phi_r-\phi_i) \tag{47}$$

We can split the circle of azimuth angles ϕ_i into two parts. For the semicircle $\phi_r - \pi/2 < \phi_i < \phi_r + \pi/2$, no horizon cutoff occurs since the surface becomes self-shadowed ($\theta_i' > \pi/2$) before $\theta_e = \pi/2$. On the other hand, for the semicircle $\phi_r + \pi/2 < \phi_i < \phi_r - \pi/2$ horizon cutoff does occur and must be included in the integral for scene radiance.

Substituting this into the integral for scene radiance, we obtain

$$L_r = \frac{L_0(k+1)}{2\pi}\cos^{k-1}\theta_r \int_{-\pi}^{\pi}\int_{0}^{\min[\theta_i',\pi/2]} \cos^k\theta_i\sin\theta_i\,d\theta_i\,d\phi_i \tag{48}$$

Let $\phi = (\phi_i - \phi_r)$ and let $\phi' = (\phi_i - \phi_r) + \pi$ to split the integral with respect to ϕ_i into two parts

$$L_r = \frac{L_0(k+1)}{2\pi}\cos^{k-1}\theta_r \int_{-\pi/2}^{\pi/2}\int_0^{\pi/2}\cos^k\theta_i \sin\theta_i \, d\theta_i \, d\phi + \frac{L_0(k+1)}{2\pi}\cos^{k-1}\theta_r \int_{-\pi/2}^{\pi/2}\int_0^{\theta_i'}\cos^k\theta_i \sin\theta_i \, d\theta_i \, d\phi' \tag{49}$$

Now,

$$\int_0^{\pi/2}\cos^k\theta \sin\theta d\theta = \frac{1}{k+1} \tag{50}$$

so the first term is simply $(L_0/2)\cos^{k-1}\theta_r$. The remaining term is more difficult to evaluate.

$$\int_0^{\theta_i'}\cos^k\theta \sin\theta d\theta = \frac{[1-\cos^{k+1}\theta_i']}{k+1} \tag{51}$$

so that the second terms becomes

$$\frac{L_0}{2\pi}\cos^{k-1}\theta_r \int_{-\pi/2}^{\pi/2}[1-\cos^{k+1}\theta_i']d\phi' = \frac{L_0}{2\pi}\cos^{k-1}\theta_r \left[\pi - 2\int_0^{\pi/2}\cos^{k+1}\theta_i' \, d\phi'\right] \tag{52}$$

where $\cot\theta_i' = \tan\theta_r\cos\phi'$ indicates the dependency between θ_i' and ϕ'. One can solve for $\cos\theta_i'$ to obtain

$$\cos\theta_i' = \frac{\sin\theta_r\cos\phi'}{\sqrt{1-\sin^2\theta_r\sin^2\phi'}} \tag{53}$$

Combining the two terms, one obtains

$$L_r = L_0\cos^{k-1}\theta_r \left[1 - \frac{\sin^{k+1}\theta_r}{\pi}\int_0^{\pi/2}\left[\frac{\cos\phi}{\sqrt{1-\sin^2\theta_r\sin^2\phi}}\right]^{k+1} d\phi\right] \tag{54}$$

It does not appear that the solution for L_r can be expressed in terms of elementary functions with k a free parameter. The solution can be expressed, however, in terms of the Gamma function $\Gamma(z)$ and the hypergeometric series $F(\alpha,\beta;\gamma;z)$. Applying integral 3.681(1) of Gradshteyn & Ryzhik (1965), one obtains

$$\int_0^{\pi/2}\left[\frac{\cos\phi}{\sqrt{1-\sin^2\theta_r\sin^2\phi}}\right]^{k+1} d\phi = \frac{1}{2}\frac{\Gamma(\frac{1}{2})\Gamma(\frac{k+2}{2})}{\Gamma(\frac{k+3}{2})} F(\tfrac{k+1}{2},\tfrac{1}{2};\tfrac{k+3}{2};\sin^2\theta_r) \tag{55}$$

where

$$\Gamma(z) = \int_0^\infty e^{-t}\ t^{z-1}\ dt \tag{56}$$

and

$$F(\alpha,\beta;\gamma;z) = 1 + \frac{\alpha\cdot\beta}{\gamma\cdot 1}z + \frac{\alpha(\alpha+1)\beta(\beta+1)}{\gamma(\gamma+1)\cdot 1\cdot 2}z^2 + \frac{\alpha(\alpha+1)(\alpha+2)\beta(\beta+1)(\beta+2)}{\gamma(\gamma+1)(\gamma+2)\cdot 1\cdot 2\cdot 3}z^3 + \cdots \tag{57}$$

Absolute convergence of the hypergeometric series $F(\alpha,\beta;\gamma;z)$ is assured when $|z| < 1$ and $\mathrm{Re}(\alpha + \beta - \gamma) < 0$. These conditions are satisfied for all choices of k and θ_r. Recalling that $\theta_n = \theta_r$, we obtain

$$L_r = L_0\cos^{k-1}\theta_n \left[1 - \frac{\sin^{k+1}\theta_n}{2\pi}\left[\frac{\Gamma(\frac{1}{2})\Gamma(\frac{k+2}{2})}{\Gamma(\frac{k+3}{2})}\ F(\tfrac{k+1}{2},\tfrac{1}{2};\tfrac{k+3}{2};\sin^2\theta_n)\right]\right] \tag{58}$$

For any choice of k, this equation can be used to numerically generate a table of values for L_r as a function of the single variable θ_n. The expression involving $\Gamma(z)$ determines a constant independent of θ_n. For each value of θ_n, terms of the hypergeometric series $F(\alpha,\beta;\gamma;z)$ can be expanded and summed to the desired degree of numerical accuracy.

For some choices of k, equation (58) reduces to an expression involving elementary functions. For the case $k = 0$, result 9.121(13) of Gradshteyn & Ryzhik (1965) gives

$$F(\tfrac{1}{2},\tfrac{1}{2};\tfrac{3}{2};\sin^2\theta_n) = \frac{\theta_n}{\sin\theta_n} \tag{59}$$

so that

$$L_r = \frac{L_0}{\cos\theta_n}\left[1 - \frac{\theta_n}{\pi}\right] \tag{60}$$

For the case $k = 1$, result 9.121(24) of Gradshteyn & Ryzhik (1965) gives

$$F(1,\tfrac{1}{2};2;\sin^2\theta_n) = \frac{2(1 - \sqrt{1 - \sin^2\theta_n})}{\sin^2\theta_n} \tag{61}$$

so that

$$L_r = L_0 \left[\frac{1 + \cos\theta_n}{2} \right] \tag{62}$$

Both the cases $k = 0$ and $k = 1$ can be derived more easily by direct solution of the required integral, but are demonstrated here as special cases of the general method.

Solar Irradiance at the Top of the Atmosphere						
Landsat MSS:						
Band	4	5	6	7		
Wavelength Interval (μm)	.5 - .6	.6 - .7	.7 - .8	.8 - 1.1		
Percentage of Solar Constant	13.1	11.2	9.1	18.4		
Solar Irradiance[1] ($mW \cdot cm^{-2}$)	17.7	15.1	12.4	24.9		
Landsat TM:						
Band	1	2	3	4	5	7
Wavelength Interval (μm)	.45 - .52	.52 - .60	.63 - .69	.76 - .9	1.55 - 1.75	2.08 - 2.35
Percentage of Solar Constant	10.2	10.3	6.6	10.8	3.3	1.6
Solar Irradiance[1] ($mW \cdot cm^{-2}$)	13.9	13.9	8.9	14.6	4.5	2.1

[1] based on solar constant of 135.3 $mW \cdot cm^{-2}$. This value is considered accurate to ± 2.1 $mW \cdot cm^{-2}$ for a quiet sun at the mean sun-to-earth distance. It is estimated that the solar constant varies from 130.9 $mW \cdot cm^{-2}$ at aphelion to 139.9 $mW \cdot cm^{-2}$ at perihelion.

Table 1. Values of solar irradiance for a quiet sun at the top of the atmosphere at the mean sun-to-earth distance, for Landsat satellites. TM band 6 (10.4 - 12.5 μm) is not included since there is neglible solar irradiance at the top of the atmosphere in this wavelength interval. The table is derived from standard ANSI/ASTM E 490 - 73a "Solar constant and air mass zero solar spectral irradiance tables", proposed in (Thekaekara (1970)) and adopted in 1973, in slightly modified form, by ASTM Committee E-21 on Space Simulation and Applications of Space Technology. The value for each Landsat band is obtained by integrating the standard solar spectral irradiance curve over the specified wavelength interval.

Estimated Atmospheric Parameters						
	$L_P(z)$		$E_S(z)$		$\tau(z)$	
	L_{P0} mW·cm^{-2}·sr^{-1}	H_P m	E_{S0} mW·cm^{-2}	H_S m	τ_0	H_τ m
Method I (Sept)	0.521	3406	3.00	3406	0.262	2529
Method I (Jan)	0.173	1592	3.00	1592	0.262	2529
Method II (Jan)	0.173	1592	3.66	1129	0.494	9196
Method III (Jan)	0.173	1592	1.21	9838	0.365	2000

(a)

Estimated Atmospheric Parameters						
	$L_P(z)$ mW·cm^{-2}·sr^{-1}		$E_S(z)$ mW·cm^{-2}		$\tau(z)$	
	944m	2684m	944m	2684m	944m	2684m
Method I (Sept)	0.395	0.237	2.27	1.36	0.180	0.091
Method I (Jan)	0.096	0.032	1.66	0.56	0.180	0.091
Method II (Jan)	0.096	0.032	1.59	0.34	0.446	0.377
Method III (Jan)	0.096	0.032	1.10	0.94	0.228	0.095

(b)

Table 2. Estimated atmospheric parameters. In (a) the results are given for path radiance, sky irradiance and optical thickness in terms of sea-level ($z = 0$) values and a corresponding scale height. In (b) the results are given in terms of values estimated for the range of elevations that actually occur in the St. Mary Lake test site.

Values of Relief Displacement				
Satellite Sensor	Nominal Altitude (km)	Maximum Scan Angle (degrees)	Nominal Pixel Spacing (m)	Elevation Change for 1 Pixel Displacement (m)
Landsat 1,2,3 MSS	902	5.78	58	507
Landsat 4,5 MSS	705	7.47	58	406
Landsat 4 TM (Bands 1,2,3,4,5,7)	705	7.47	30	210
Landsat 4 TM (Band 6)	705	7.47	120	840
SPOT MLA (nadir mode)	820	2.12	20	472
SPOT MLA (off-nadir mode)	820	28.12	26	44
SPOT PLA (nadir mode)	820	2.12	10	236
SPOT PLA (off-nadir mode)	820	28.12	13	22
Seasat SAR	820	20.00	25	11

Table 3. Values of relief displacement for the Landsat, SPOT and Seasat satellite sensors, from (Wong (1984)). Included are the Multispectral Scanner (MSS) and Thematic Mapper (TM) of Landsat, the Multispectral Linear Array (MLA) and Panchromatic Linear Array (PLA) of SPOT and the Synthetic Aperture Radar (SAR) of Seasat.

Estimates of the Minnaert coefficient k						
Date	Sun		k			
	el	az	band 4	band 5	band 6	band 7
17/Sep/79	37.8	146.6	0.27	0.55	0.78	0.99
25/Sep/74	35.2	149.2	0.22	0.47	0.77	1.05
08/Jan/79	13.8	153.1	1.06	1.58	1.59	1.72

Table 4. Estimates of the Minnaert coefficient k for each Landsat MSS band from images acquired over St. Mary Lake on three different dates.

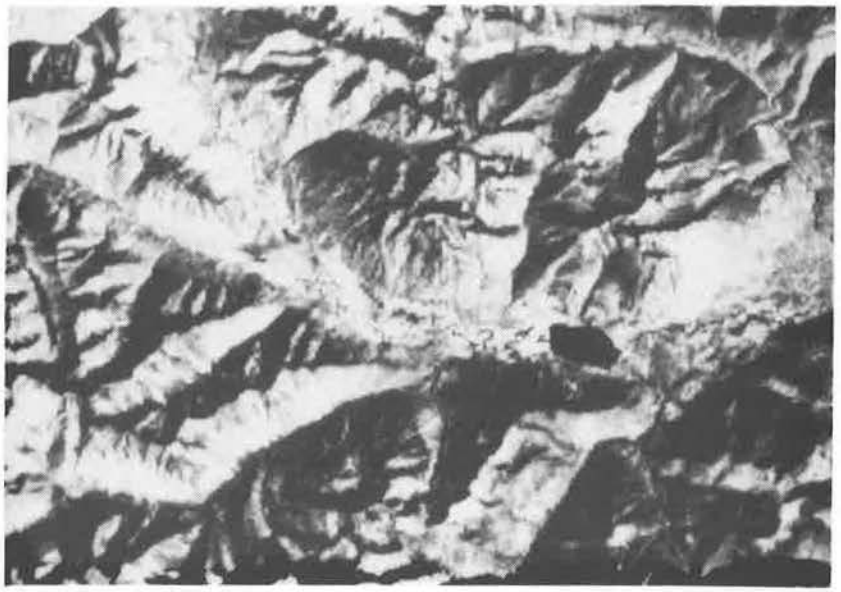

(a)

(b)

Figure 1. A portion of Landsat MSS band 7 (frame-id 30561-17560), acquired 17:56 GMT on September 17, 1979, is shown in (a). At the time of image acquisition, the sun was at an elevation of 37.8 degrees and an azimuth of 146.6 degrees, measured clockwise from north. A Lambertian surface with uniform ground cover illuminated by a collimated source with identical elevation and azimuth is shown in (b). The correlation coefficient between (a) and (b), excluding points in shadow and on flat terrain, is 0.737.

(a)

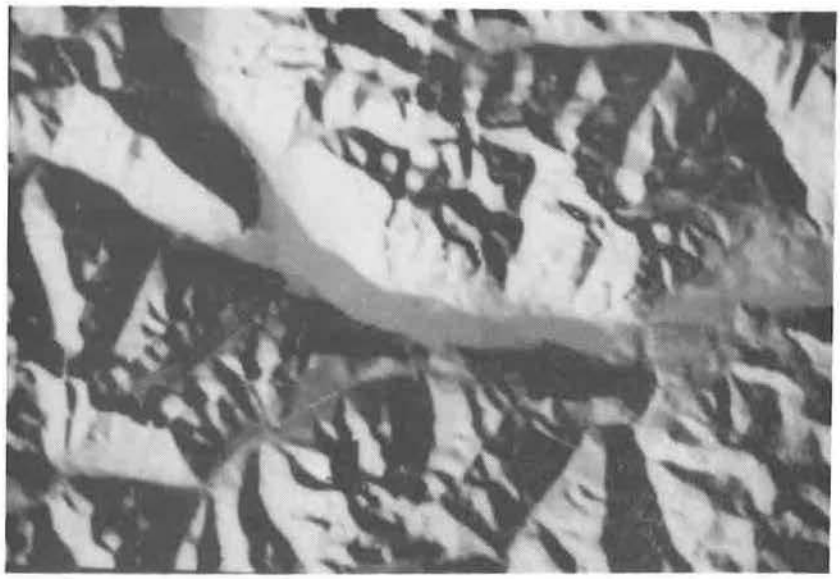

(b)

Figure 2. Comparing Lambertian surfaces for different times of day. At 17:56 GMT on September 17, 1979 the sun was at an elevation of 37.8 degrees and an azimuth of 146.6 degrees, measured clockwise from north. The corresponding Lambertian surface with uniform ground cover is shown in (a). Five hours later the sun was at elevation of 26.9 degrees and an azimuth of 238.0 degrees. The corresponding Lambertian surface with uniform ground cover is shown in (b). The correlation coefficient between (a) and (b), excluding points in shadow, is -0.049.

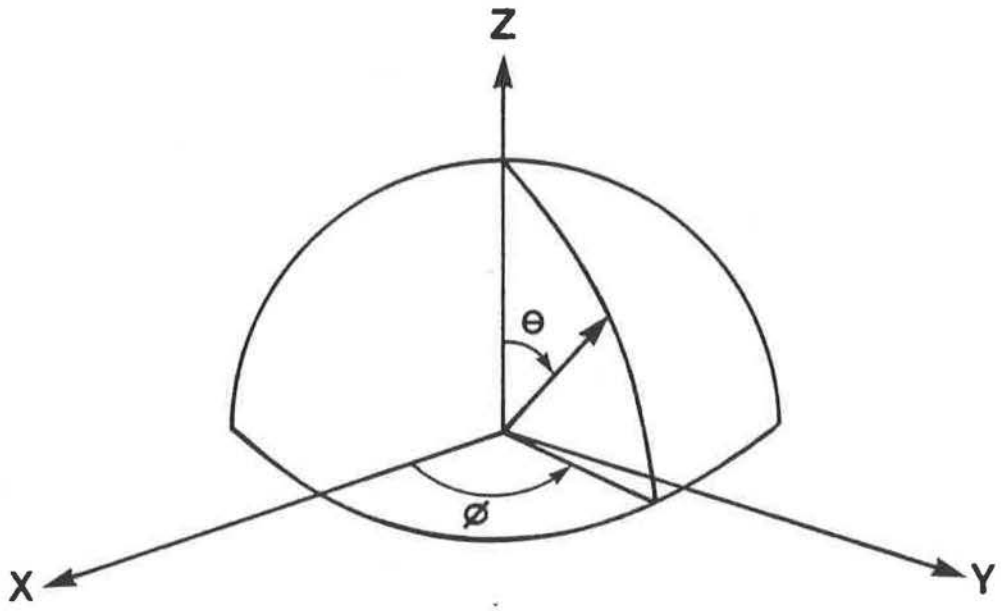

Figure 3. Directions can be represented by points on the unit sphere. The polar or zenith angle θ is measured from the Z-axis and the azimuth angle ϕ is measured counter-clockwise from the X-axis in the XY plane.

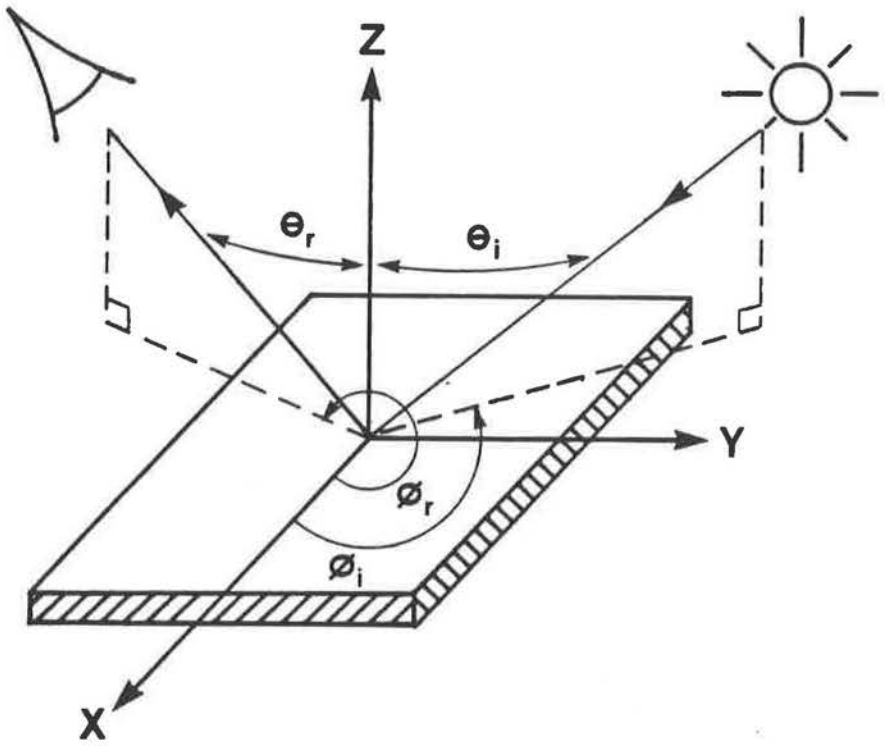

Figure 4. The local geometry of the incident and the reflected ray can be specified by spherical coordinates (θ_i, ϕ_i) and (θ_r, ϕ_r).

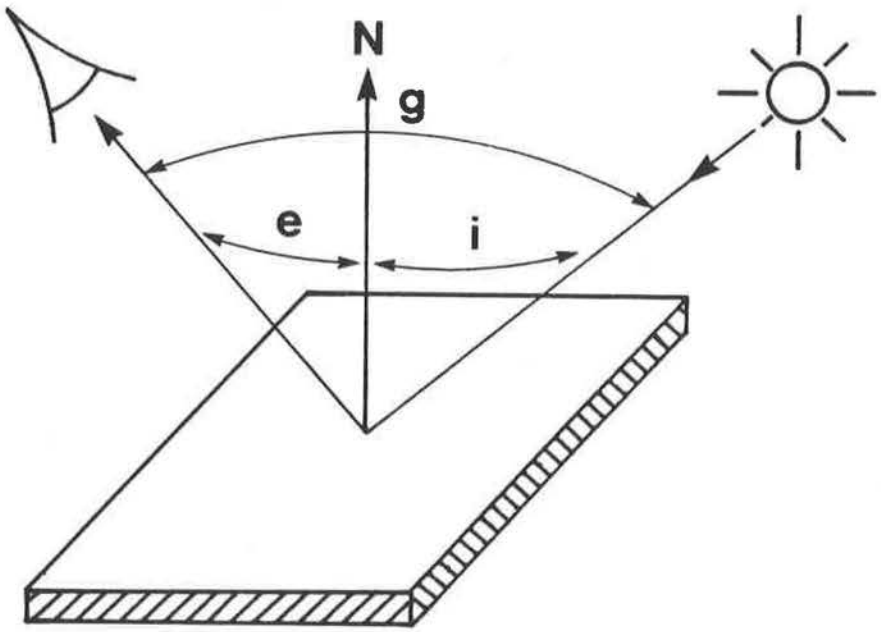

Figure 5. For isotropic materials, the local geometry of the incident and the reflected ray can be specified by three angles i, e and g. The incident angle i is the angle between the incident ray and the surface normal. The exitant angle e is the angle between the reflected ray and the surface normal. The phase angle g is the angle between the incident and reflected rays.

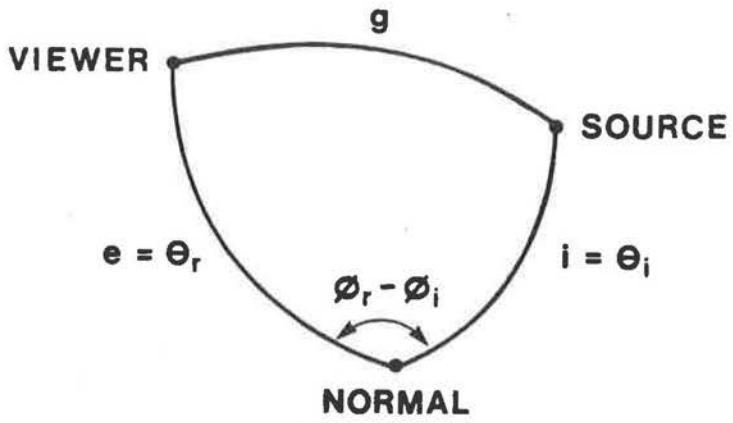

Figure 6. Spherical triangle used to derive the transformation between spherical coordinates (θ_i,ϕ_i) and (θ_r,ϕ_r) and the angles i, e and g.

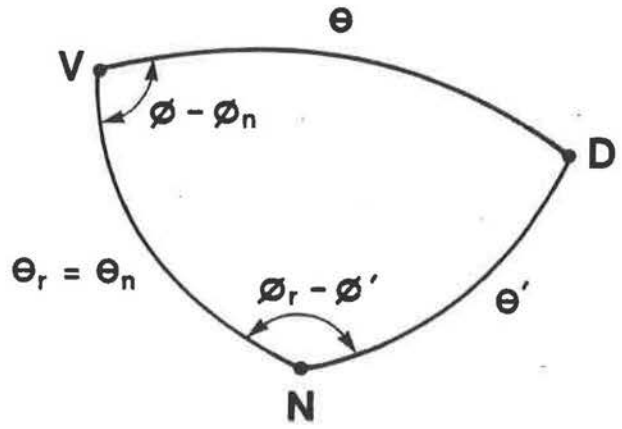

Figure 7. Spherical triangle used to derive the transformation between one spherical coordinate system and another. Here, (θ',ϕ') are the object-centred coordinates and (θ,ϕ) the viewer-centred coordinates of an arbitrary direction D.

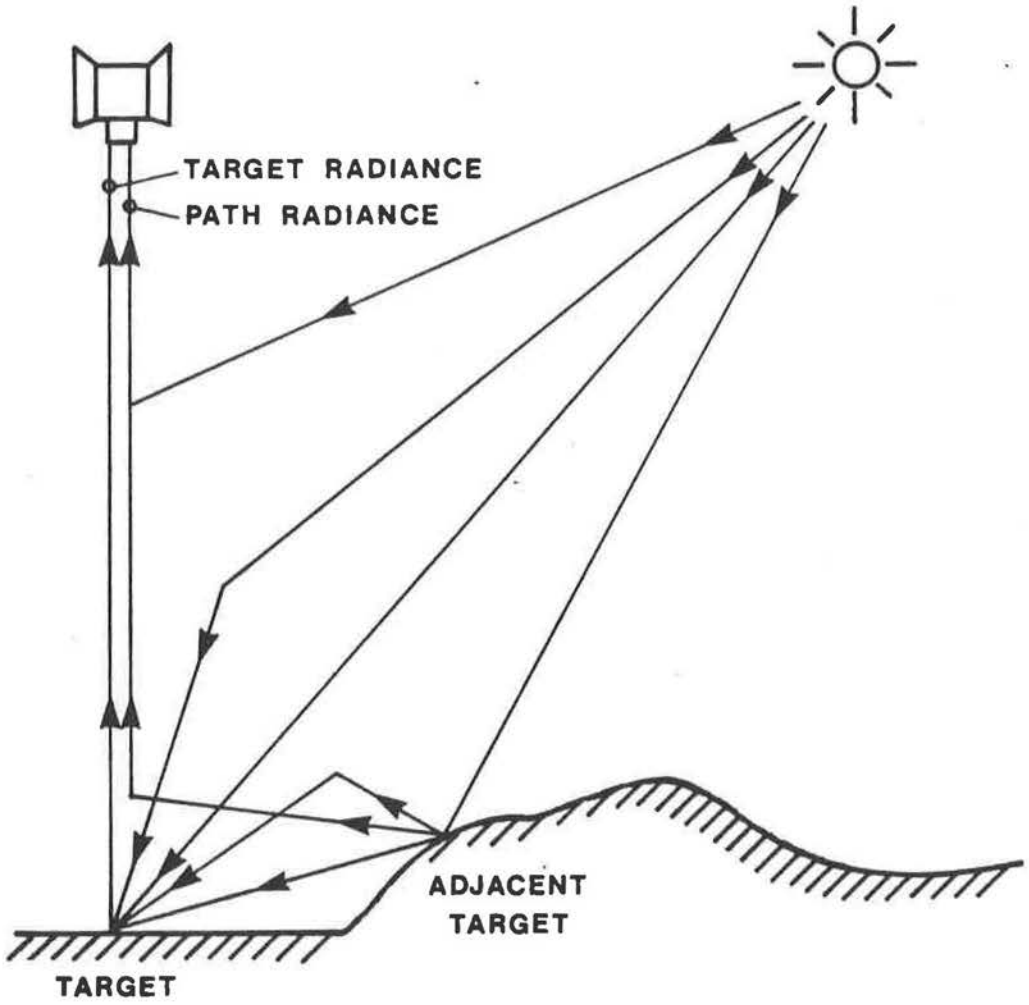

Figure 8. Components of scene radiance in remote sensing. The target receives direct solar radiation and diffuse sky radiation. Diffuse sky radiation has components due to scattered solar radiation and radiation from adjacent targets that is reflected directly or scattered back to the target. The sensor measures scene radiance that includes an additional path radiance component of radiation not originating from the target. Path radiance includes radiation scattered to the sensor from the solar beam and from radiation reflected from adjacent targets.

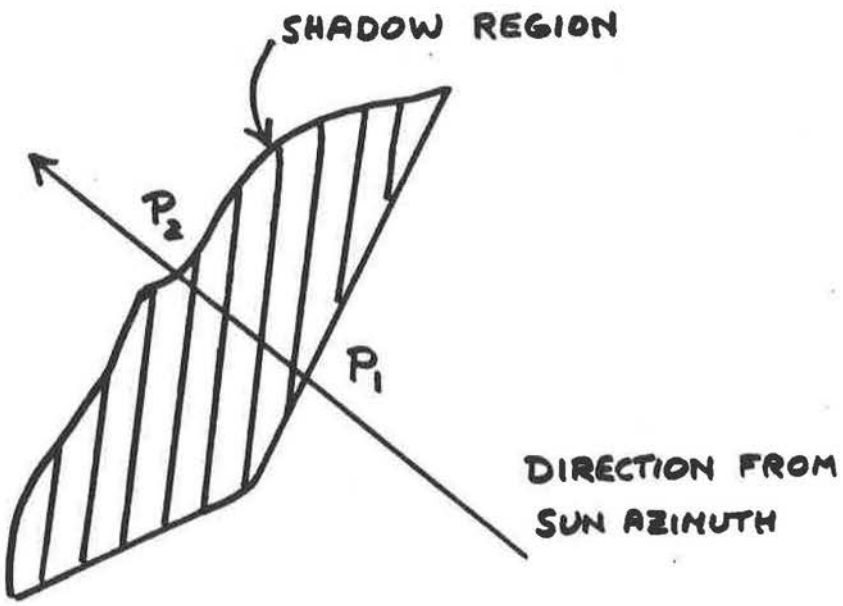

Figure 9. Method II considers points across shadow boundaries. Shadow regions are traversed from the direction of sun azimuth. At P_1 the transition is from light to dark. At P_2 the transition is from dark to light.

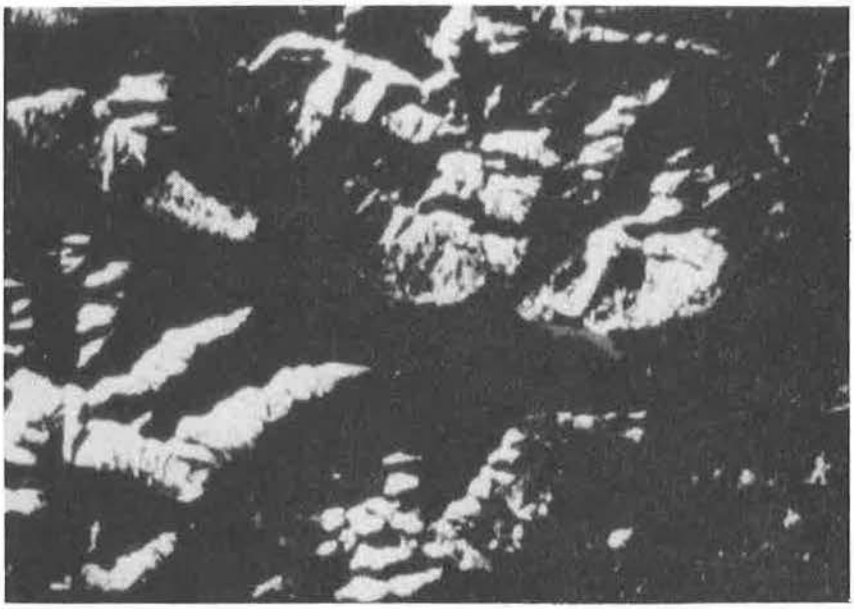

(a)

(b)

Figure 10. A portion of Landsat MSS band 7 (frame-id 30309-17574), acquired 17:58 GMT on January 8, 1979, is shown in (a). At the time of image acquisition, the sun was at an elevation of 13.8 degrees and an azimuth of 153.1 degrees, measured clockwise from north. A Lambertian surface with uniform ground cover illuminated by a collimated source with identical elevation and azimuth is shown in (b). The correlation coefficient between (a) and (b), excluding points in shadow and on flat terrain, is 0.635.

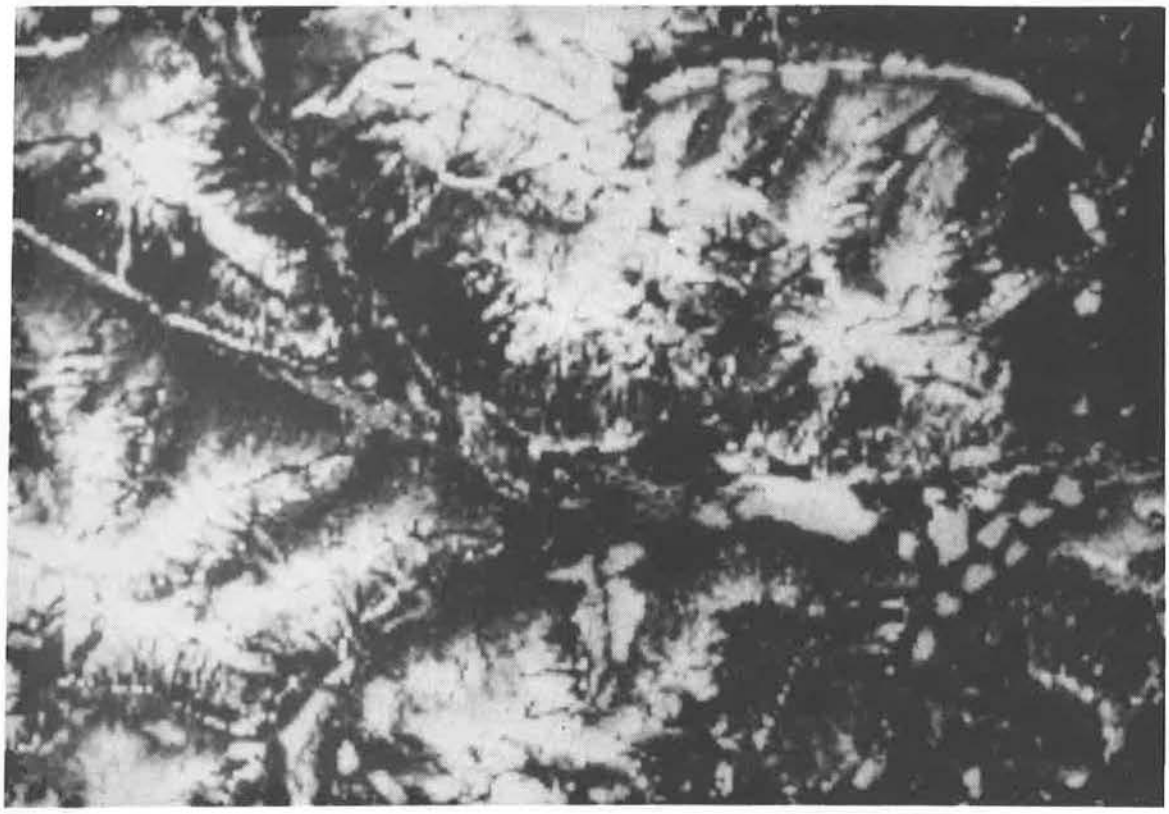

Figure 11. Albedo map for band 4 of January 8, 1979 Landsat MSS image. This albedo was generated using the atmospheric parameters estimated by Method III.

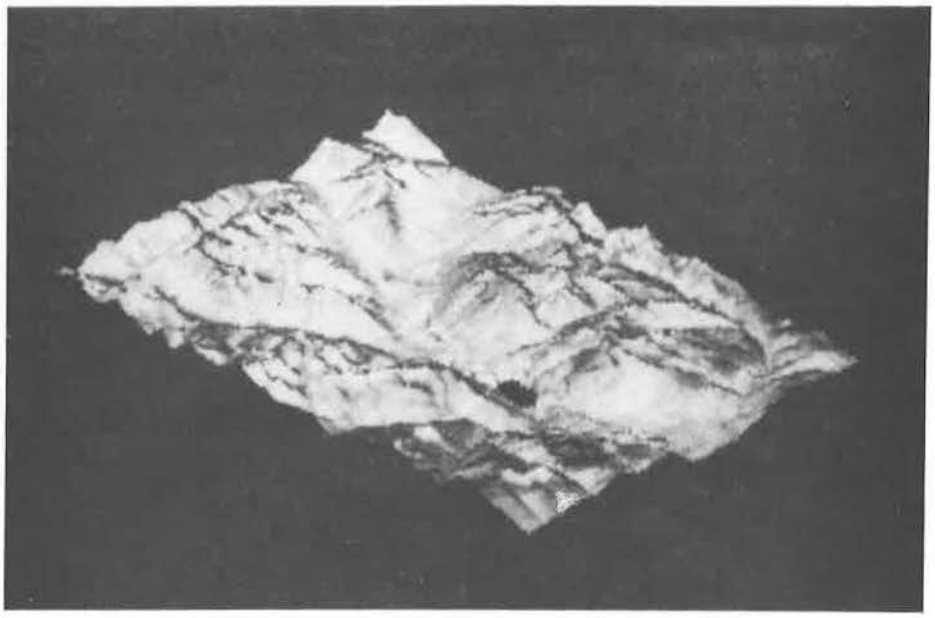

Figure 12. Synthetic oblique view.

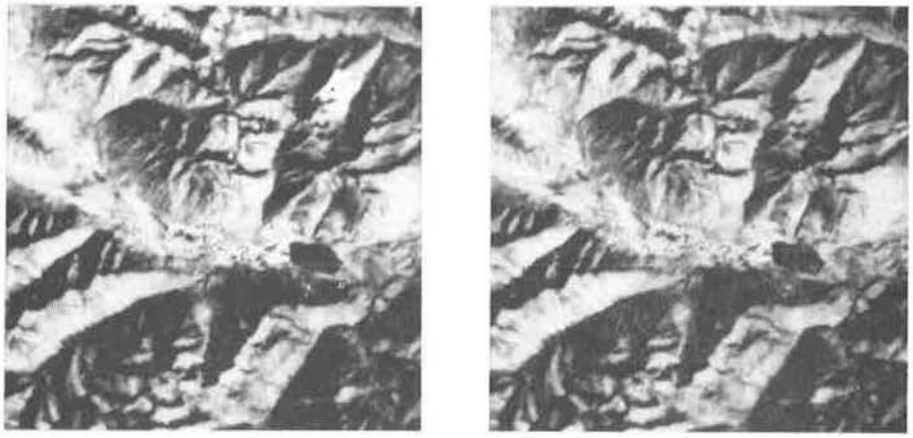

Figure 13. Synthetic stereo pair. A pocket lens stereoscope is recommended in order to view this figure in stereo.

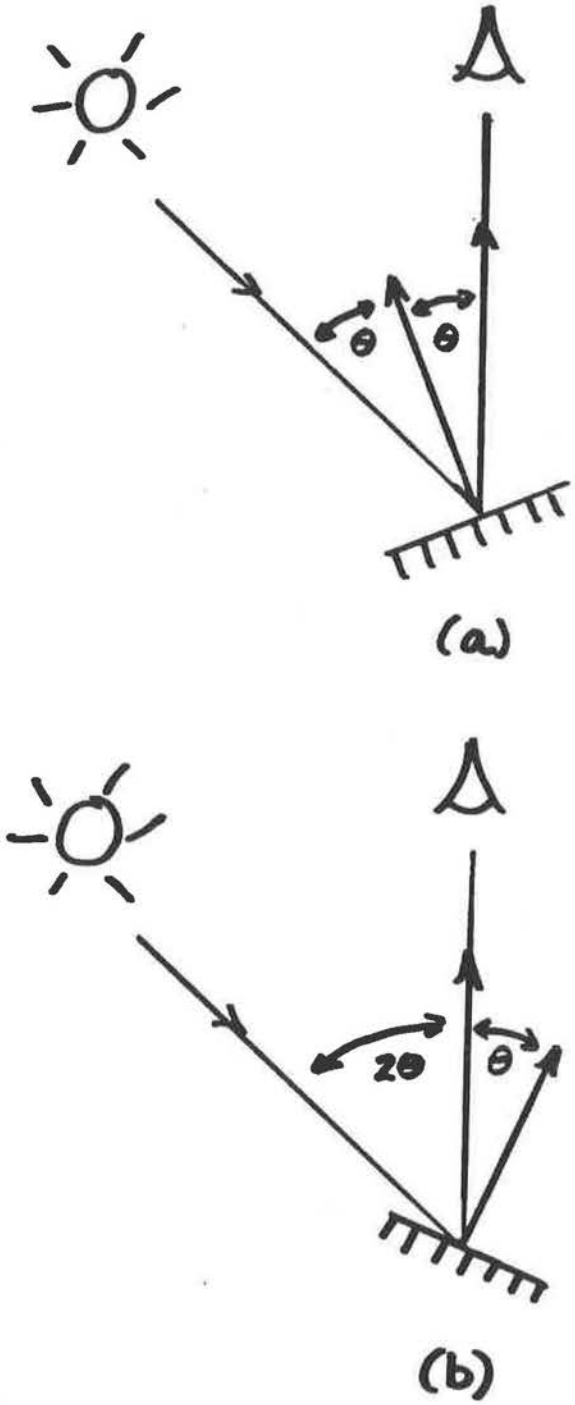

Figure 14. In (a) the surface is viewed with $i = e = \theta$. In (b) the surface is viewed with $i = 3\theta$ and $e = \theta$. Going from (a) to (b) corresponds to rotating the surface about the fixation point through an angle of 2θ in the plane of the source and viewer.

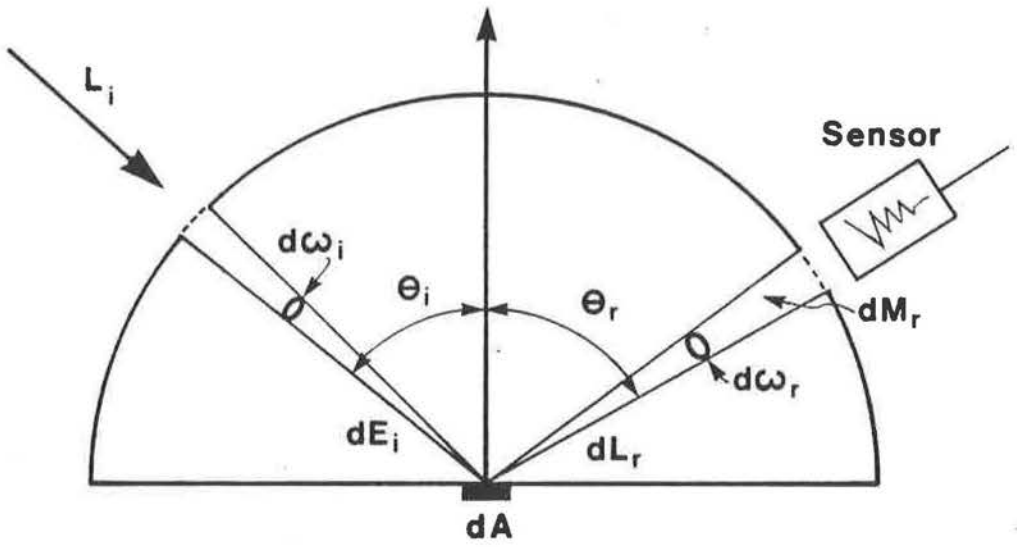

Figure 15. Configuration for phenomenological derivation of the BRDF.